Available online at www.sciencedirect.com

ScienceDirect

Geochimica et Cosmochimica Acta 304 (2021) 191–215

Geochimica et Cosmochimica Acta

www.elsevier.com/locate/gca

The role of sulfides in the chalcophile and siderophile element budget of the subducted oceanic crust

Jesse B. Walters [a,b,*], Alicia M. Cruz-Uribe [a], Horst R. Marschall [b], Brandon Boucher [c]

[a] School of Earth and Climate Science, University of Maine, Orono 04469, United States
[b] Institut für Geowissenschaften, Goethe Universität, Frankfurt am Main 60438, Germany
[c] Department of Earth Sciences, University of New Brunswick, Fredericton E3B 5A3, Canada

Received 25 November 2020; accepted in revised form 8 April 2021; Available online 28 April 2021

Abstract

Subduction zones are the site of long-term chemical cycling between Earth's surface and interior. During subduction, dehydration and melting may partition mobile elements into the overlying mantle wedge and arc system. Volcanic arcs also host much of the world's base (*e.g.*, Cu, Sn, Sb, and Mo) and precious (*e.g.*, Au, Ag) metal deposits. However, slab contributions to the chalcophile and siderophile element (CSE) budget of arc magmas and their associated ore deposits remain controversial. Although previous studies have identified the mobility of some CSE in slab fluids, few studies have examined the contribution from sulfides to the CSE budget of the slab. Here we report *in situ* laser ablation inductively coupled plasma mass spectrometry (LA-ICP-MS) analyses of Cr, Co, Ni, Cu, Zn, Ga, Ge, As, Mo, Ag, Cd, In, Sn, Sb, Te, Tl, Pb, and Bi in sulfides and silicates in thirteen rocks from six exhumed high-pressure (HP) terranes worldwide. Combined with data from the literature, we demonstrate that sulfides host nearly the entire Cu, As, Ag, Cd, and Te budget of subducted rocks, whereas Co, Ni, Zn, Ga, Ge, Mo, Sn, and Tl are dominantly hosted in silicate and oxide phases. Prograde sulfide-breakdown during subduction is expected to liberate Cu, As, Ag, Cd, and Te into the overlying arc-mantle wedge system, whereas Co, Ni, Zn, Ga, and Pb may be partially lost during lawsonite, epidote, and amphibole dehydration reactions. In contrast, Ge, Tl, Sn, and Mo are largely retained in the eclogitic slab residue. We also demonstrate that CSE zoning in pyrite may be used to track high pressure (HP) metasomatism. Oscillatory Co and Ni zoning in metasomatic pyrite is linked to transitions between fluid and rock buffered regimes, consistent with seismic- and dehydration-induced cyclic fluctuations in fluid pore pressure and flux. Thus, minor and trace CSEs in HP rocks may also be a useful tool to constrain slab fluid migration.

Keywords: Chalcophile; Siderophile; Subduction; LA-ICP-MS; Sulfide; In-situ; High-pressure; Metamorphic

1. INTRODUCTION

Subduction zones are home to much of the world's base (*e.g.*, Cu, Sn, Sb, and Mo) and precious (*e.g.*, Au, Ag) metal ore deposits (*e.g.*, Richards, 2011). Magmatic-hydrothermal deposits are associated with arc magmas that exhibit both slab and subarc mantle components (*e.g.*, Ellam and Hawksworth, 1988; Marschall and Schumacher, 2012; Plank and Langmuir, 1993). Elements that fractionate from the slab residuum during dehydration migrate to the slab-mantle interface, are eventually introduced to the mantle wedge and may migrate to the crust during arc magmatism (*e.g.*, Bebout et al., 1999; Spandler and Pirard, 2013). Alternatively, slab or mélange melting may directly transfer slab components into arc magmas (Cruz-Uribe et al., 2018; Marschall and Schumacher,

* Corresponding author at: Institut für Geowissenschaften, Goethe Universität, Frankfurt am Main 60438, Germany.
E-mail address: Walters@em.uni-frankfurt.de (J.B. Walters).

https://doi.org/10.1016/j.gca.2021.04.016
0016-7037/

2012; Spandler and Pirard, 2013). Incompatible chalcophile and siderophile elements (CSE; Cr, Co, Ni, Cu, Zn, Ga, Ge, As, Mo, Ag, Cd, In, Sn, Sb, Te, Tl, Pb, and Bi) are concentrated in the oceanic crust during mantle melting (see review in Lorand and Luguet, 2015), and may be further concentrated during hydrothermal seafloor alteration (*e.g.*, Patten et al., 2016a,b). In addition to other sources, such as the lithospheric mantle and lower crustal cumulates, the slab may provide a source for the CSE in arc-related ore deposits (see review in Richards, 2011; Tomkins and Evans, 2015). For example, Sillitoe (1972) attributed the orogen-perpendicular zoning of Cu ± Au, Ag + Pb + Zn, and Sn + Mo metal provinces with distance from the trench to the partial melting of subducted oceanic crust and seafloor sediments at progressively deeper levels. Studies by de Hoog et al., 2001; Noll et al., 1996; Stolper and Newman, 1994, and Timm et al. (2012) attributed enrichments of As, Sb, Pb, Cu, Mo, Zn, V, and Au in arc lavas to a slab-derived fluid source. Additionally, Tl isotopes have been linked to a slab sediment-derived component in the arc (Nielsen et al., 2016). Anomalous concentrations in arc magmas are mirrored by elevated abundances in some subarc mantle xenoliths. Metasomatized sub-arc xenoliths show elevated Au, Cu, Pt, Pd, Os, Re, As, Se, Sb, Bi, and Te relative to the depleted mantle (McInnes et al., 1999; Kepezhinskas et al., 2002; Tassara et al., 2017, 2018). Similarly, sulfides in eclogitic diamonds show an enrichment in As, Sb, Tl, Pb, and Bi, possibly from a slab-derived source, whereas no addition of Cr, Co, Ni, Cu, Ag, Sn, Mo, and W is observed (Aulbach et al., 2012). In contrast, the studies of Jenner et al. (2010), Lee et al. (2012), and Lee and Tang (2020) suggest no Cu or Au enrichment in parental arc magmas relative to mid-ocean ridge basalt (MORB). However, the lack of Cu or Au enrichment in arc magmas may reflect sulfide saturation during melting and does not necessarily preclude an enriched source. Such studies have yet to come to a consensus on the origin of CSEs in arc magmas; additionally, the extent to which these elements are extracted from the slab remains poorly constrained (Richards, 2011).

Exhumed high-pressure metamorphic rocks from fossil subduction zones provide a record of slab fluids and their trace element compositions. Natural data from high-pressure reaction zones demonstrate the mobilization of Cr, Co, Ni, Cu, Zn, As, Sb, Mo, and Pb (van der Straaten et al., 2008, 2012; Spandler et al., 2011; Guo et al., 2012; Li et al., 2013, 2017; Vitale et al., 2014; Fornash and Whitney, 2020), whereas limited mobility is observed for Ga in subduction zone fluids (van der Straaten et al., 2012; Vitale et al., 2014; El Korh et al., 2017). These data are supported by experiments, which show fluid mobility for Cr, Ni, Cu, and Pb (Kessel et al., 2005; Kogiso et al., 1997). However, the role of sulfides in CSE loss from the slab is rarely quantified. *In situ* analysis of sulfides in ore deposits demonstrate that these minerals are a major host of a wide variety of CSEs (*e.g.*, Cook et al., 2013; George et al., 2018; Reich et al., 2013; Román et al., 2019), and sulfides may play a similar role in controlling the budget of many CSEs in the slab. Despite their namesake, CSEs exhibit chalcophile to lithophile behavior in many lithospheric systems. For example, the chalcophile elements Cd, In, and Sn exhibit lithophile behavior during mantle partial melting (Yi et al., 2000), whereas highly siderophile elements (Os, Ir, Ru, Rh, Pt, Pd, Au, and Re) are incorporated into residual base metal sulfides (*e.g.*, Luguet et al., 2003; Tassara et al., 2018). Chalcophile and siderophile elements may similarly deviate from Goldschmidt's classification in subducted mafic crust; therefore, the degree to which CSE partition between sulfides, silicates, and oxides during subduction metamorphism must be quantified.

Recent studies suggest that sulfide breakdown and/or dissolution may be significant during prograde subduction metamorphism of the mafic crust (Tomkins and Evans, 2015; Walters et al., 2019; 2020; Li et al., 2020). Sulfur loss from the slab may also drive the release of sulfide-hosted CSE into slab fluids or melts. Studies by Evans et al. (2014), Crossley et al. (2018), Su et al. (2019), and Walters et al. (2019) demonstrate that pyrite precipitated within the slab and subduction channel from slab fluids exhibits significant zoning in Co, Ni, and As. *In situ* LA-ICP-MS analyses of pyrite and chalcopyrite in eclogite from the Tianshan, China, by Li et al. (2013) suggest that sulfides account for 75.7, 25.5, and 99.8% of the Co, Ni, and Cu whole-rock budgets, respectively. Sulfides are also found to contain measurable Zn (0.15–225 μg/g), As (3.30–42.2 μg/g), Se (2.92–66.7 μg/g), Mo (≤236 μg/g), Ag (≤45.1 μg/g), Au (≤0.31 μg/g), Pb (≤28.0 μg/g), Sb (≤1.81 μg/g), Te (≤7.79), and Bi (≤1.98 μg/g; Li et al., 2013). Dale et al. (2009) found that sulfides similarly dominate the Os, Ir, Ru, and Pd budget of eclogitic metagabbros, and linked the loss of Ni-rich sulfides to a prograde depletion in Pb. Chauvel et al. (1995), Kelley et al. (2005), and King et al. (2007) proposed that Pb in the slab is concentrated in sulfides during seafloor alteration and the breakdown of sulfides during prograde metamorphism will fractionate Pb from U. Over time, recycling of slab residue with elevated U/Pb may be responsible for the HIMU mantle reservoir (Chauvel et al., 1995). Consistent with these data, Bebout et al. (1999) attributed the systematic decrease in As (and Sb) with increasing metamorphic grade to sulfide breakdown during sediment subduction. The role sulfides may play in the minor and trace element budget of other CSEs, such as Ga, Cd, In, Sn, and Tl, remains unexplored. Additionally, the limited datasets above may not capture the full variability of sulfide minor and trace element compositions in exhumed high-pressure rocks.

Here we report *in situ* LA-ICP-MS data for Cr, Co, Ni, Cu, Zn, Ga, Ge, As, Mo, Ag, Cd, In, Sn, Sb, Te, Tl, Pb, and Bi in sulfides and silicates in thirteen samples of HP rocks from six exhumed terranes worldwide (Fig. 1). We combine our observations with previously published literature data and thermodynamic models to assess the impact of prograde sulfur loss and slab dehydration on the CSE budget of the subducted mafic crust. Additionally, we show detailed examples in which sulfide and silicate trace element zoning, coupled with petrographic observations, may be used to infer fluid infiltration during high-pressure metasomatism.

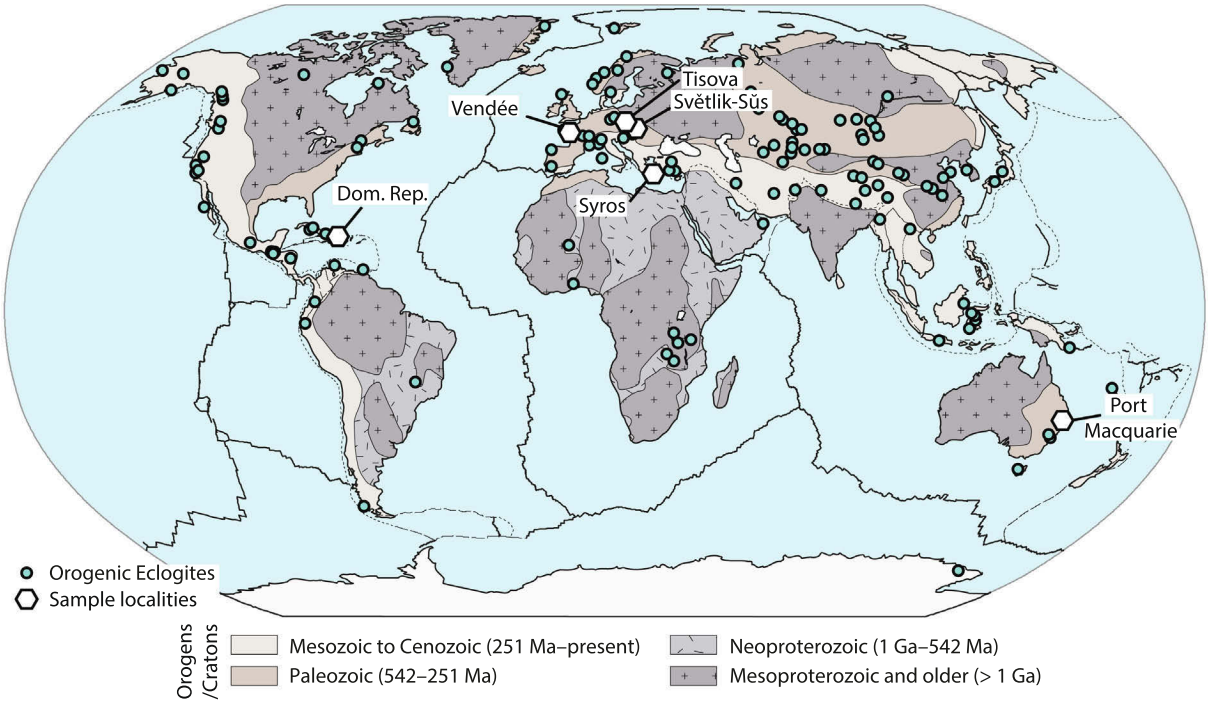

Fig. 1. Map showing our sample locations and the global distribution of orogenic eclogites. Modified with permission after Tsujimori and Mattinson (2021) and Tsujimori and Ernst (2014).

2. PETROGRAPHY AND GEOLOGIC BACKGROUND

The petrography and geologic background of the studied samples are described in detail in Walters et al. (2019). Here we present an overview and detail new relevant insights. All mineral abbreviations in figures and tables follow Whitney and Evasns, 2010, except thiospinel (Tsp, see discussion below) and white mica (Wm). Samples used in this study are classified in terms of their tectonic history into two groups (Tables 1 and 2): those sourced from coherent lithotectonic units (Czech Republic, France) and those from mélange zones (Greece, Dominican Republic, and Australia). Sample locations are shown in Fig. 1.

2.1. Coherent units

Samples from coherent lithotectonic units (Table 1) exhibit similar assemblages and textures. These samples are variably retrogressed eclogites of Variscan age (350–450 Ma; Peucat et al., 1982; Faryad et al., 2013; Collett et al., 2018). Estimates of the peak eclogite facies metamorphic *P-T* conditions for rocks from the Světlik-Sůs, Tisova, and Vendee localities are 2.0–2.4 GPa and 746 ± 27 °C, 1.6–1.8 GPa and 640–715 °C, 1.6–2.0 GPa and 650–750 °C, respectively (O'Brien and Vrána, 1995; O'Brien, 1997; Jelínek et al., 1997; Štědrá, 2001; Brandelik and Massonne, 2004; Faryad et al., 2006; Godard, 2009). Granulite-facies overprints of the samples from Světlik-Sůs and Tisova are estimated at 1.7 GPa and ~780 °C and 1.2 GPa and 800–850 °C, respectively (O'Brien and Vrána, 1995; O'Brien, 1997; Jelínek et al., 1997; Brandelik and Massonne, 2004; Faryad et al., 2006). More recently, Collett et al. (2018) proposed peak eclogite facies conditions of 2.5 GPa and 650–750 °C followed by granulite facies metamorphism at 1.4–1.8 GPa and >800 °C for the Tisova eclogites. Durations of <1 Ma for HT metamorphism of eclogites from Světlik-Sůs and Tisova are calculated by garnet diffusion chronometry (O'Brien and Vrána, 1995;

Table 1
Mineralogy of samples from coherent lithotectonic units.

Locality	Peak *P–T* (GPa, °C)	Sample	Rock type	Minerals present (high to low relative abundance)
Vendee, FR	1.6–2.0, 650–750	G083-12	Eclogite	Grt, Omp, Sdn/Prg, Di, Qz, Pl, Chl, Rt, Ilm, Ttn, Py, Ccp, Tsp
Světlik-Sůs, CZ	2.0–2.4, 746 ± 27	SVS-11-01	Retrogressed eclogite	Grt, Omp, Di, Pl, Sdn/Prg, Ap, Rt, Ilm, Ttn, Py, Ccp, Po, Tsp, Hc, Mag
Tisova, CZ	1.6–1.8, 640–715	TIS-11-02	Retrogressed eclogite	Grt, Omp, Di, Pl, Sdn/Prg, Qz, Rt, Py, Ccp, Po, Czo/Ep, Tsp, Ap

Table 2
Mineralogy of mélange samples.

Locality	Peak P–T (GPa, °C)	Sample	Rock type	Minerals present (high to low relative abundance)
Jagua Clara M., DR	1.3–2.5, 360–800	DR1203-07-02	Jadeitite	Jd, Pl, Cal, Qz, Chl, Wm, Ttn, Ep, Py, Ccp, Gn
		DR1203-10-02	Blueschist	Gln, Brs, Ep, Pmp, Omp, Wm, Chl, Ttn, Po, Ccp, Pl, Ap
		DR1203-11-03	Grt blueschist	Grt, Gln, Act, Wm, Ep, Ttn, Pl, Qz, Py, Rt, Brt, Gp, Co-Ni sulfide, Cct, Cv, Ccp
		DR1203-15-02	Chl schist	Chl, Ap, Py, Ilm, Zrn
Port Mac., AU	2.9, 600	PMQ06-5	Blueschist	Gln, Omp, Wm, Ttn, Chl, Py, Ccp, Po
Syros, GR	2.2 ± 0.2, 530 ± 30	SY328	Omp-Chl fels	Chl, Omp, Ilm, Ap, Py, Ccp, Bn
		SY404	Chl schist	Chl, Tr, Ap, Ttn, Py, Mag, Zrn, Rt, Ilm
		SY462	Grt-Omp-Chl fels	Grt, Omp/Aeg, Ap, Ilm, Rt, Ep/Aln, Py, Ccp, Cct, Ktp
		SY523	Chl schist	Chl, Tlc, Act, Py, Ap

O'Brien, 1997), whereas the geochronologic estimates of Collett et al. (2018) suggest a 15 Ma duration for Tisova.

The coherent lithotectonic samples have a peak assemblage of garnet + omphacite + rutile ± quartz. Omphacite is partially to completely replaced by symplectite of calcic clinopyroxene + albitic plagioclase, whereas garnets are enclosed by thin rims of kelyphite, consisting of calcic plagioclase + green clinoamphibole (Fig. 2A). The kelyphitic amphiboles in all three samples grade into massive clinoamphibole. Sulfide inclusions are observed in garnet in all three samples. In G083-12, sulfide inclusions are pyrite + chalcopyrite, whereas in SVS-11-01 and TIS-11-02 inclusions are chalcopyrite + pyrrhotite ± pentlandite. Retrograde metasomatic sulfides are present in all three samples (Walters et al., 2019). In samples SVS-11-02 matrix pyrite is rimmed by chalcopyrite + pyrrhotite, whereas pyrite in TIS-11-02 is rimmed by a corona of chalcopyrite followed by pyrrhotite (Fig. 2B). In addition to inclusions of peak phases, such as garnet, omphacite, and rutile, pyrite grains also contain abundant inclusions of retrograde phases. For example, clinopyroxene + plagioclase symplectites are included in pyrite in SVS-11-01, and inclusions of clinoamphibole, clinozoisite-epidote, and titanite are observed in pyrite from TIS-11-01 and TIS-11-02. Chalcopyrite and pyrrhotite grains contain inclusions of small (<10 μm) thiospinel grains ($Me^{2+}Me_2^{3+}S_4$, where Me = Co,Ni,Fe). In G083-12, large xenoblastic pyrite are overgrown by a second generation of dendritic pyrite (Fig. 2C). Small chalcopyrite grains are present on pyrite surfaces, and thiospinel grains are associated with late chlorite and albite plagioclase (Fig. 2C).

2.2. Tectonic Mélange

Samples from tectonic mélanges (Table 2) exhibit a wide range of mineral assemblages, textures, P–T conditions, and tectonic histories. Samples from mélange zones were collected from the Jagua Clara mélange, Dominican Republic; the island of Syros, Greece; and Port Maquarie, Australia.

The Jagua Clara mélange in the Dominican Republic hosts blocks of blueschist, eclogite, jadeitite, peridotite, orthogneiss, and metapelitic rocks in an antigorite serpentinite matrix that has been variably converted to chlorite-talc schist (Krebs et al., 2008, 2011; Schertl et al., 2012; Escuder-Viruete et al., 2013). Estimates of peak metamorphic conditions range from 1.3 to 2.5 GPa and 360 to 800 °C depending on the peak assemblage and both clock-wise and counterclockwise P–T paths have been proposed for different blocks (Krebs et al., 2008, 2011; Escuder-Viruete and Pérez-Estaún, 2013). Samples of sulfide-bearing blueschist, garnet blueschist, chlorite schist, and jadeitite are included in our study (Table 2).

On the island of Syros, Greece, a single clockwise P–T path with peak eclogite facies conditions of 2.2 ± 0.2 GPa and 530 ± 30 °C are proposed for metamorphosed mafic, felsic, and volcaniclastic blocks in a serpentinite matrix (Laurent et al., 2018). Estimates of 0.6–1.3 GPa and 350–450 °C have been proposed for some blackwall mineral assemblages (Breeding et al., 2004; Marschall et al., 2006; Miller et al., 2009). Samples are blackwall lithologies, including chlorite schist, chlorite-omphacite fels (an isotropic rock), and garnet-omphacite-chlorite fels.

The mélange at Port Macquarie, Australia, hosts blocks of blueschist, omphacitite, glacophanite, and folded and interlayered blueschists with rare enclaves of lawsonite eclogite (Och et al., 2003; Nutman et al., 2013; Tamblyn et al., 2019). Tamblyn et al. (2020) estimated approximate peak metamorphic conditions of 2.9 GPa and 600 °C, followed by partial exhumation to less than 2.0 GPa and 500 °C and reburial to ~2.7 GPa and ~590 °C. A single sample of sulfide-rich interlayered blueschist (Fig. 2G) is included in this study (Table 2).

Mélange zone samples are divided into those that are from block interiors, which largely preserve their protolith bulk rock composition, and those that are hybrid metasomatic 'blackwall' rocks (Table 2). Samples DR1203-11-03 is the only sample taken from a block interior. It is a texturally well equilibrated garnet blueschist, which exhibits a peak assemblage of garnet + actinolite + glaucophane + white mica + epidote (Fig. 2D). Garnet grains contain small inclusions of clinopyroxene replacing plagioclase, whereas rare matrix albite is associated with pyrite. Pyrite, pyrrhotite, chalcopyrite, and a fine-grained Co-Ni-Fe sulfide phase, too small to be identified by EDS, occur in the matrix and infilling cracks within garnet (Walters et al.,

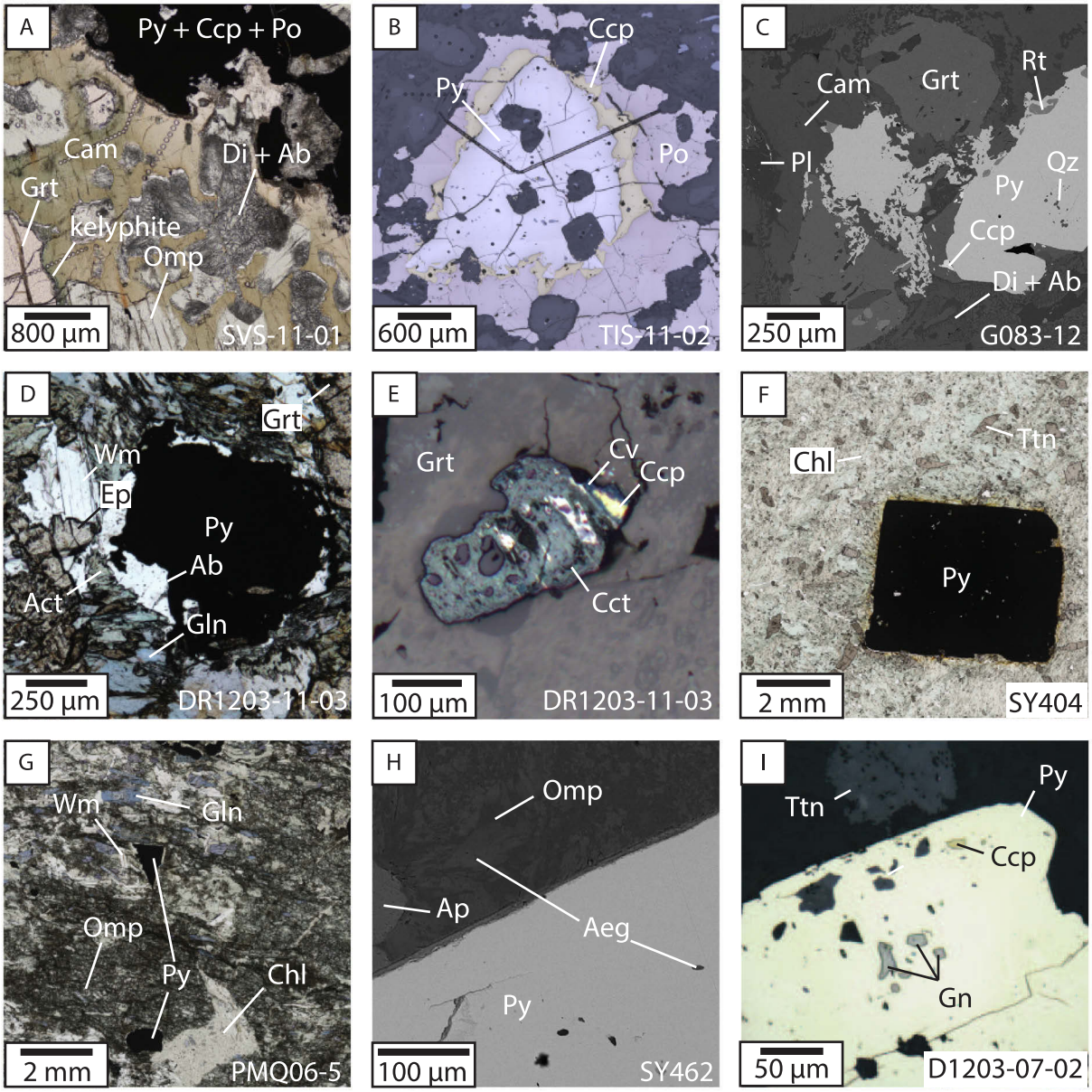

Fig. 2. Transmitted (A, D, F, G), reflected (B, E, I), and back scattered electron (C, H) images of key mineral textures. Figures A-C show large sulfide grains associated with clinoamphibole and diopside + albite symplectite in retrogressed eclogite from coherent units. Figures D–I show textures in samples from mélange zones: glaucophane, actinolite, albite, epidote, white mica, and garnet adjacent to a pyrite mass in DR1203-11-03 (D), inclusion of fine grained chalcocite and covellite after chalcopyrite in garnet in DR1203-11-03 (E), pyrite in a mass of chlorite and titanite in SY404 (F), glaucophane, white mica, omphacite, and chlorite with pyrite cross cutting the foliation of the banded blueschist sample PMQ06-5 (G), pyrite with aegirine inclusions in sample SY462 (H), pyrite with inclusions of chalcopyrite and galena in DR1203-07-02 (I).

2019). Additionally, pyrite, chalcopyrite, and an inclusion of covellite (CuS) and chalcocite (Cu_2S) replacing chalcopyrite was observed in garnet (Fig. 2E, Walters et al., 2019).

Hybrid samples (DR1203-07-02, DR1203-10-02, DR1203-15-02, SY328, SY404, SY462, SY523, PMQ06-5) display a wide variety of mineral assemblages and textures (Table 2), including nearly monomineralic rocks such as jadeitite (Fig. 2I; DR1203-07-02) and chlorite schists (Fig. 2F; DR1203-15-02, SY404), rocks exhibiting an isotropic texture and eclogite-like assemblage (Fig. 2H; SY462), and a sample with thin-section scale compositional banding (Fig. 2G; PMQ06-5). Pyrite is the dominant sulfide in most samples, with or without minor chalcopyrite. Notable exceptions include pyrrhotite + chalcopyrite masses within a vein of pumpellyite + omphacite + chlorite + w hite mica in blueschist sample DR1203-10-02, galena and chalcopyrite inclusions in pyrite from jadeitite sample DR1203-07-02 (Fig. 2I), bornite (Cu_5FeS_4) inclusions in

pyrite from sample SY328, and chalcocite inclusions in ilmenite in sample SY462 (Walters et al., 2019). Hydrous minerals such as chlorite, epidote/allanite, and clinoamphibole are commonly included in sulfides, linking sulfide precipitation and blackwall formation (Walters et al., 2019). In the more mineralogically complex blackwall samples, multiple generations of overprinting metasomatic textures are commonly observed. For example, clinopyroxene grains in SY462 display aegirine cores and Na-rich omphacite rims (Fig. 2H). Overprinting textures in sulfides are also observed in PMQ06-5, where pyrite grains are misaligned with or cut the foliation (Walters et al., 2019).

3. METHODS

3.1. Major and minor element analysis

Samples were prepared as 1-in. (2.54 cm) round polished sections or epoxy grain mounts.

Major and minor element data for silicates and sulfides were collected using the electron probe microanalyzer (EPMA) facilities at the University of Maine and Goethe Universität. Mineral compositional data are summarized in Tables EA1–EA2 and the analytical facility used is noted for each analysis. Data are reported as the mean and 2SE of ten closely spaced analyses within the same chemical zone; however, <10 analyses are averaged for small or intensely zoned grains. Calculations of garnet and clinopyroxene structural formulae, including Fe^{3+} determination, were done using method two of Schumacher (1991). Amphibole structural formula calculations follow Leake et al. (1997); however, amphiboles were classified following the recent IMA approved classification scheme of Hawthorne et al. (2012). Structural formulae of other elements were determined by standard normalization schemes utilizing either an assumed number of cations or anions where appropriate, and the method used is indicated in Tables EA1 and EA2.

Instrumentation at the University of Maine consists of a Cameca SX100 EPMA equipped with four wavelength dispersive spectrometers (WDS). A 15 kV accelerating voltage and 10 nA beam current with a 5 μm spot size was used for all analyses. Backgrounds were measured for 10 s and on-peak counting times were 20 s, except for Na, where counting times were 5 s and 10 s for background and peak, respectively. The set of natural and synthetic standards used for calibration were jadeite (Na), diopside (Mg, Si, Ca), rutile (Ti), magnetite (Fe), rhodonite (Mn), sanidine (K, Al), and Cr_2O_3 (Cr) for most silicates, except for white mica and chlorite for which tugtupite and anorthite were used for Na and Al, respectively.

Further, analyses at Goethe Universität were collected using a JXA-8530F Plus Hyperprobe field-emission EPMA equipped with five WDS carrying H- and L-type spectrometer crystals. Operating conditions were a 15 kV accelerating voltage, 20nA beam current, and a 3 μm spot size for all silicates, except for white mica and chlorite, for which a 10 μm spot size was used. Operating conditions for sulfide analyses were a 20 kV accelerating voltage, 20nA beam current, and 3 μm spot size. Detection limits for Co, Ni, and As in sulfides are 116–125 μg/g, 128–142 μg/g, and 75–87 μg/g, respectively. For silicate analyses, peak counting times were 40 s for Si and Mg, 30 s for K and Ti, and 20 s for Al, Cr, Fe, Mn, Ca, and Na, whereas counting times were 80 s for S and As, 60 s for Si, 50 s for Ni, 40 s for Co and Cu, and 30 s for Fe for sulfide analyses. Background counting times were half of their respective on-peak counting times (*e.g.*, 20 s for Si). The set of natural and synthetic standards used for calibration were albite (Na), forsterite (Mg), fayalite (Fe), wollastonite (Ca, Si), pyrophanite (Mn), Cr_2O_3 (Cr), Al_2O_3 (Al), and $KTiO(PO_4)$ (K, Ti, P) for silicate analyses. For sulfide analyses a natural pyrite standard was used for S, whereas pure metal standards were used for Fe, Co, Ni, As, Cu, and Si.

3.2. X-ray intensity maps

Qualitative X-ray intensity maps were collected using the EPMA at the University of Maine. Garnet maps collected with a 20 kV accelerating voltage, 100 nA beam current, and a dwell time of 30 ms. Sulfide Co, Ni, and As X-ray intensity maps from Walters et al. (2019) are reproduced here.

3.3. Minor and trace element analysis

Minor and trace element analyses were collected at the laser ablation inductively coupled plasma mass spectrometry (LA-ICP-MS) facility housed in the Department of Earth Sciences, University of New Brunswick, Canada. This facility is equipped with an Australian Scientific Instruments Resolution™ M-50 193 nm ArF excimer laser. The laser is equipped with a two-volume low-volume Laurin Technic Pty S-155 large format sample cell. The cell was repeatedly evacuated and backfilled with He following each sample exchange. Ablated material was transported to an Agilent 7700x single collector quadrupole ICP-MS by 300 mL/min ultra-pure He carrier gas. The sample stream was mixed downstream of the cell with 2 mL/min N_2 and 930 mL/min Ar before reaching the plasma torch. For spot analyses the Laurin Technic Pty signal smoothing device ('squid') was used to decrease the relative standard deviation of the measured signal during ablation; however, this device was removed during raster analyses. At the beginning of the session the ICP-MS was tuned while rastering across NIST610 glass. Oxide production was monitored with ThO^+/Th^+, which was kept below 0.2%, and double-charged ion production monitored with $^{44}Ca^{++}/^{44}Ca^+$ was kept below 0.3%.

Twenty-one isotopes were monitored (^{29}Si, ^{34}S, ^{52}Cr, ^{56}Fe, ^{59}Co, ^{60}Ni, ^{63}Cu, ^{66}Zn, ^{71}Ga, ^{73}Ge, ^{75}As, ^{95}Mo, ^{107}Ag, ^{111}Cd, ^{115}In, ^{118}Sn, ^{121}Sb, ^{125}Te, ^{205}Tl, ^{208}Pb, and ^{209}Bi) during sulfide analyses with an additional two isotopes (^{27}Al and ^{43}Ca) monitored during silicate analyses. Sulfide spot analyses were conducted using a ~2 J/cm^2 laser beam energy density (fluence), 3 Hz repetition rate, and a 33 μm spot size. Ablations were conducted for 45 s followed by 30 s gas blanks. Silicates were run with the same parameters, except for an increased beam energy density of ~3 J/cm^2. A total of 78 sweeps were measured per analysis

with approximately 6 s of washout. Sulfide rasters were conducted using a laser energy density of 1.5 J/cm^2, repetition rate of 10 Hz, and 33 μm spot size at a raster speed of 8 μm/s.

Time resolved signals were processed using the trace element data reduction scheme in Iolite™ version 2.5 (Paton et al., 2011). Iron was used as an internal standardization element for sulfide analyses, and Si was used for silicate phases. The USGS reference material MASS-1 sulfide pressed powder (Wilson et al., 2002) was used as the primary reference material to convert mass fractions to elemental concentrations in sulfides. Quality control materials for sulfide analyses were NIST SRM610 glass (Pearce et al., 1997; Jochum et al., 2011), BCR-2G glass (GeoReM database), and Po724 pyrrhotite (Memorial University, Newfoundland). For analyses of silicate minerals, NIST SRM610 was used as the primary reference material and BCR-2G was analyzed as a quality control material.

Analytical sessions consisted of one analysis of each reference material interspersed between every 5–18 unknown analyses, depending on the length of the analytical session. External 2σ reproducibility and GeoReM preferred values are reported in Table EA3. Typical 2σ external reproducibility of secondary reference materials is <10% for concentration ranges of 10–100's of μg/g and <50% for elements <10 μg/g. Despite unmatched matrices between the primary pressed sulfide powder reference material (MASS-1) and glass secondary reference materials (NIST610, BCR-2G), measured values typically reproduce the accepted values within uncertainty (see Electronic Annex). Analyses were carefully examined for inclusions, down-hole zoning, and crossing grain boundaries into other phases. Copper surface contamination was apparent in some pyrite analyses; where observed the first 10 seconds were not considered. Only the first portions of zoned analyses are reported so as to better correlate to minor element maps and mineral textures in 2D. Analyses were also monitored for potential interferences. Potential interferences of Na (e.g., $^{40}Ar^{23}Na^+$, $^{23}Na_2^{16}OH^+$, $^{23}Na_2^{17}O$) and Ti (e.g., $^{47}Ti^{16}O^+$, $^{46}Ti^{17}O$) on ^{63}Cu, and ^{115}Sn on ^{115}In were identified (see Electronic Annex); therefore, Cu and In concentrations are not considered in our interpretations for minerals with high concentrations of the respective interfering element.

Sulfide minor and trace element data are presented in Table EA4, and silicate data are presented in Table EA5. Internal standard values are reported in Table EA6 and average detection limits and associated 2SE are reported in Table EA7.

4. EPMA RESULTS

Major and minor element data from EPMA analyses are summarized in Table EA1 for sulfides and Table EA2 for silicates. Qualitative sulfide and garnet X-ray intensity maps are shown in Figs. EA1–EA22 and EA23–EA26, respectively. These data are summarized below.

4.1. Sulfides

Pyrite shows a relatively restricted compositional range, with only Co, Ni, and As rarely reaching the wt% level (Table EA1). Cobalt concentrations in pyrite range from below detection (<116–125 μg/g) to 3.32 wt% Co in the rim of a pyrite grain in TIS-11-02. A comparison of EPMA and LA-ICP-MS Co concentrations show a nearly 1:1 correspondence within analytical uncertainty (Fig. EA27), suggesting a limited contribution from the Fe Kα peak. Nickel concentrations range from below detection (<128–142 μg/g) to 0.40 ± 0.01 wt% Ni in G083-12. Arsenic concentrations are typically below detection (<75–87 μg/g); however, concentrations up 0.58 wt% As were measured in pyrite from PMQ06-5.

Qualitative minor element maps show a variety of Co, Ni, and As zones, which are discussed in Walters et al. (2019) and summarized here (see Figs. EA1–EA22). Pyrite from blackwall samples (DR1203-15-02, PMQ06-5, SY404, SY462, SY523) in many cases displays fine oscillatory zoning in Co, whereas zoning in Ni is less commonly observed (*e.g.*, Fig. EA28). Cobalt and arsenic concentrations correlate in sample PMQ06-5, where elevated Co-As rich cores are followed by finer scale oscillatory zoning in Co and Ni in the mantles and rims (Fig. 3 & EA29). In the jadeitite sample (DR1203-07-02), two generations of pyrite are separated by a high-Co annulus (Fig. EA2). Pyrite in eclogite samples SVS-11-01 and TIS-11-02 exhibits sharp high-Co low-Ni rims (*e.g.*, Fig. EA22). In sample G083-12, an early generation of large xenoblastic pyrite shows variable zoning in Co and Ni, whereas a second generation of dendritic pyrite is Co-Ni poor (Fig. EA9).

Pyrrhotite compositions range from $Fe_{0.867}S$ in samples DR1203-10-02 and TIS-11-02 to $Fe_{0.907}S$ in sample SVS-11-01. Ni concentrations are consistently above the detection limit and range from 0.23 to 0.52 wt% Ni. Chalcopyrite analyses are stochiometric and do not display Co, Ni, and As concentrations above detection limits. Preliminary maps of pyrrhotite and chalcopyrite did not show visible minor element zoning and are not considered here.

Small thiospinel grains were analyzed in samples G083-12 and SVS-11-01, but were too small in TIS-11-02 for a clean analysis. The analyzed thiospinel grains fall between greigite ($Fe^{2+}Fe_2^{3+}S_4$), linnaeite ($Co^{2+}Co_2^{3+}S_4$), polydymite ($Ni^{2+}Ni_2^{3+}S_4$), siegenite ($Co^{2+}Ni_2^{3+}S_4$), and violarite ($Fe^{2+}Ni_2^{3+}S_4$). In G083-12, thiospinel compositions range from $Fe_{0.519}Co_{0.893}Ni_{1.619}$ to $Fe_{0.280}Co_{1.417}Ni_{1.249}$. A single measured grain of a thiospinel inclusion in pyrrhotite from SVS-11-01 has the composition $Fe_{0.799}Co_{0.544}Ni_{1.715}$. In addition, one inclusion of Co-rich pentlandite in garnet was analyzed in SVS-11-01. This grain has the composition $(Fe_{3.43}Ni_{3.76}Co_{1.59})S_8$.

4.2. Silicates

Qualitative major element maps for sulfide-bearing garnet are presented in Figures EA23–EA26. Garnet in the studied samples has a variety of compositions (Table S.2)

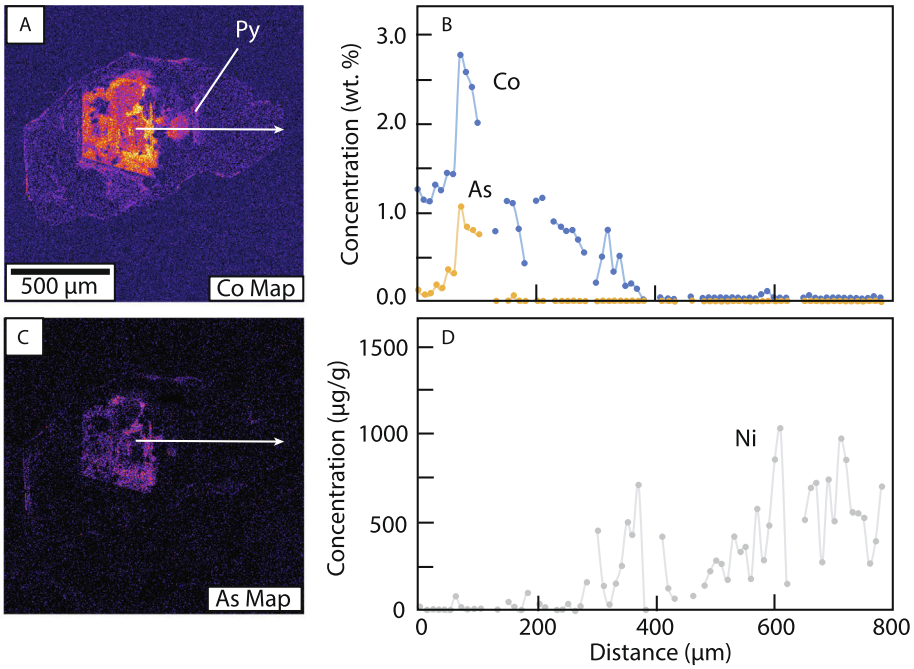

Fig. 3. Cobalt and As X-ray intensity maps of pyrite from PMQ06-5 (A, C) with EPMA transects from core to rim of Co, As, and Ni (B,D). The white line in A and C indicates the path of the transect with the arrow indicating the direction. Analyses which intersected silicate inclusions were removed. X-ray intensity maps are from Walters et al. (2019).

and major element zoning patterns (Fig. EA30). Eclogite and blueschist garnet compositions fall between $Alm_{42}Prp_{29}Sps_2Grs_{26}Adr_2$ and $Alm_{62}Prp_7Sps_2Grs_{27}Adr_2$. Garnet in eclogite from coherent units (e.g., SVS-11-01, TIS-11-02, G083-12) exhibits limited zoning (<10% endmember fraction; EA33). Garnet from the eclogitic blackwall sample (SY462) exhibits even less zoning compared to the true eclogite samples, with a near constant composition of $Alm_{64}Prp_8Sps_3Grs_{22}Adr_4$. In contrast, garnet in the blueschist sample (DR1203-11-03) shows significant core to rim zoning, with core compositions of $Alm_{44}Prp_2Sps_{17}Grs_{37}$ and rim compositions of $Alm_{60}Prp_7Sps_1Grs_{32}$ (Fig. EA30A).

Clinopyroxene is typically omphacite with compositions falling between Jd_{30} and Jd_{50}. Notable exceptions are jadeite (DR1203-07-02), aegirine (SY462), and diopside (G083-12, SVS-11-01, and TIS-11-02; see Fig. EA2). Sample SY462 shows the widest single-grain compositional variation, with clinopyroxene exhibiting cores with $Aeg_{59}Jd_{18}Quad_{23}$ and rims of $Aeg_{30}Jd_{45}Quad_{25}$. Diopside occurs in symplectite with albitic plagioclase after omphacite in eclogite samples from coherent lithotectonic units.

Amphibole grains span a range of sodic, sodic-calcic, and calcic compositions (see Fig. EA31). In eclogite samples from the coherent lithotectonic units, matrix calcic amphibole range from pargasitic in composition at the contact with sulfide grains to sadanagaite or taramite more distally. Amphibole grains in mélange samples are glaucophane, winchite, tremolite, and actinolite (Fig. EA31). A single grain of kataphorite was identified as an inclusion in epidote in sample SY462 and appears rare. In the garnet blueschist sample (DR1203-11-03), actinolite and glaucophane are in textural equilibrium within the matrix, whereas in the blueschist sample (DR1203-10-02) winchite cores are overgrown by later glaucophane (Fig. 2). Tremolite was identified in the chlorite schist sample SY404.

Minor and accessory minerals include white mica, epidote, pumpellyite, plagioclase, and titanite. White mica grains are identified as phengite and fall between $Mus_{40.4}Cel_{59.2}$ and $Mus_{54.1}Cel_{39.8}$, with less than 5% of the paragonite, trioctohedral, and pyrophyllite components. Chlorite compositions are chamosite to clinochlore and fall between $Clc_{31.5}Sud_{2.5}Ame_{24.2}Dph_{41.2}$ and $Clc_{87.0}Sud_{0.0}Ame_{0.0}Dph_{18.5}$. Clinochlore was found in chlorite schist blackwall samples,

whereas chamosite is more common in other lithologies. Epidote compositions range from $Ep_{46.2}$ to $Ep_{85.5}$. Pumpellyite observed in sample DR1203-10-02 is Al rich, with Al exceeding 2 APFU. The X_{Mg} ratio ranges from 0.58 to 0.63, suggesting limited compositional variation. Albitic plagioclase was analyzed in samples DR1203-07-02 and G083-12 and confirmed by EDS in samples DR1203-11-03, SVS-11-01, and TIS-11-02. Titanite grains in sample SY404 were analyzed and found to be Fe-, Mg-, and Mn-poor, ranging from Ttn_{95} to Ttn_{97}. Titanite grains in other samples were also found to be $>Ttn_{90}$ by EDS and were not analyzed here.

5. LA-ICP-MS RESULTS

Minor and trace element compositions determined by LA-ICP-MS are given in Table EA4 for sulfides and EA5

for silicate phases. These data are detailed below and summarized graphically in Fig. 4 for sulfides and Figs. 5–6 for silicates. Analysis locations are shown in Figures EA34–EA46.

5.1. Sulfides

Pyrite is found to consistently incorporate only Co, As, Ni, and Cu at concentrations above detection limits.

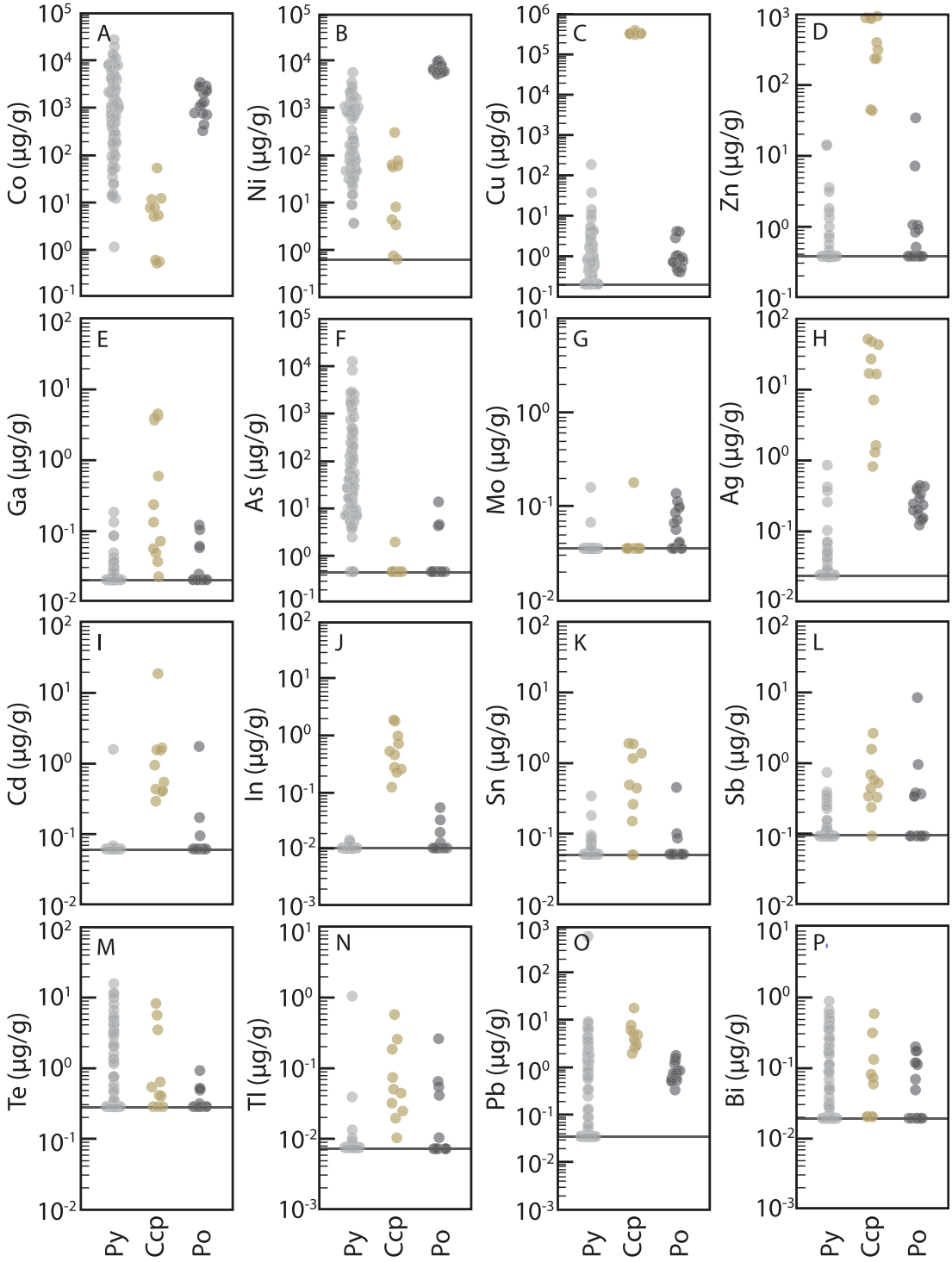

Fig. 4. Compilation of pyrite (light grey), chalcopyrite (gold), and pyrrhotite (dark grey) minor and trace element abundances. Column widths correspond to normalized frequency. Elements include Co (A), Ni (B), Cu (C), Zn (D), Ga (E), As (F), Mo (G), Ag (H), Cd (I), In (J), Sn (K), Sb (L), Te (M), Tl (N), Pb (O), and Bi (P). The dark grey line indicates the detection limit where relevant. (For interpretation of the references to colour in this figure legend, the reader is referred to the web version of this article.)

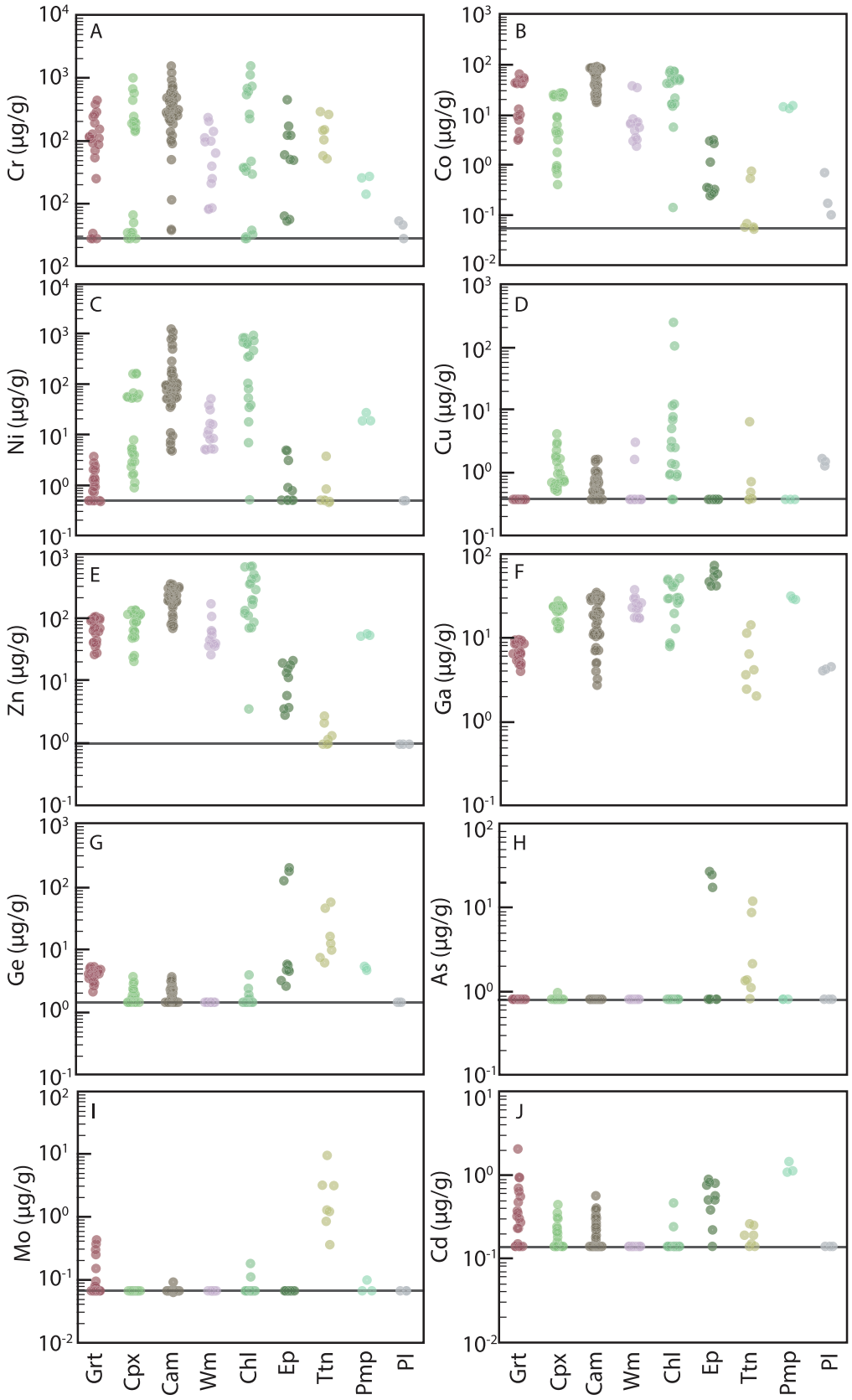

Fig. 5. Compilation of garnet (red), clinopyroxene (light green), clinoamphibole (brown), white mica (pink), chlorite (light green), epidote (dark green), titanite (yellow-green), pumpellyite (blue-green), and plagioclase (grey) minor and trace element abundances. Column widths correspond to normalized frequency. Elements include Cr (A), Co (B), Ni (C), Cu (D), Zn (E), Ga (F), Ge (G), As (H), Mo (I), and Cd (J). The dark grey line indicates the detection limit where relevant. (For interpretation of the references to colour in this figure legend, the reader is referred to the web version of this article.)

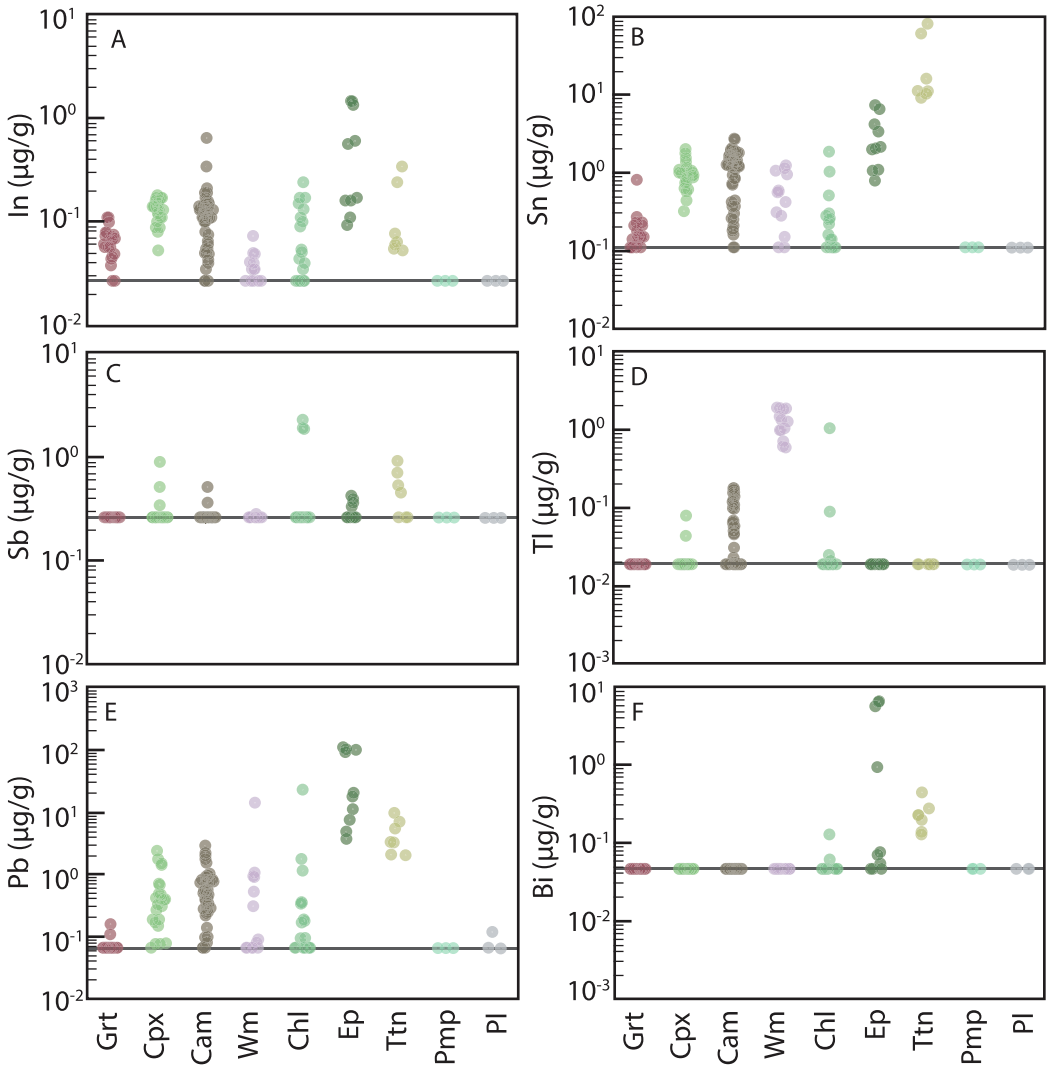

Fig. 6. Continued compilation of minor and trace element concentrations in silicate minerals. Column widths correspond to normalized frequency. Elements include In (A), Sn (B), Sb (C), Tl (D), Pb (E) and Bi (F). The dark grey line indicates the detection limit where relevant.

Cobalt, As, and Ni exhibit the highest concentrations, with maximum concentrations of 2.87 wt%, 1.27 wt%, and 0.76 wt%, respectively (Fig. 4). Cobalt and Ni concentrations are largely negatively correlated: 83% (n = 12) of Ni concentrations above 2000 µg/g occur at Co concentrations <5000 µg/g. This trend is observed in aggregate, but also evident within individual samples (*e.g.*, PMQ06-5; Fig. 7). In contrast, Co and Ni concentrations in pyrite are uncorrelated in chlorite schist samples DR1203-15-02 and SY404 (Fig. 8). The majority of other elements analyzed are below their respective detection limits with some exceptions. Interestingly, Te, Pb, and Bi are all above their detection limit in pyrite analyses from the blueschist blackwall sample PMQ06-5. Detection limits are only exceeded in a few percent of the total analyses for the elements Cr, Zn, Ga, Mo, Ag, Cd, In, Sn, Sb, and Tl.

Pyrrhotite contains consistently measurable levels of Co, Ni, Cu, Ag, and Pb (Fig. 4). The compositional range observed is more restricted for each element when compared to that of pyrite in samples where both phases are present. Cobalt concentrations range from 329 to 3510 µg/g, whereas Ni concentrations are 0.68–1.36 wt% (Fig. 4). No correlations were observed between Co and Ni in pyrrhotite; however, sample-to-sample variations are evident (Fig. 7B). Copper, Ag, and Pb concentrations are 0.52–4.15 µg/g, 0.12–0.43 µg/g, and 0.35–1.91 µg/g, respectively. Most analyses of Cr, Ga, Mo, Cd, In, Sn, Te, Tl, and Bi are below detection.

Chalcopyrite was found to incorporate Co, Ni, Zn, Ga, Ag, Cd, In, Sn, Sb, Te, Tl, and Pb. Zinc (43.2–937 µg/g) is the most abundant trace element in chalcopyrite. Cobalt and Ni concentrations are significantly lower than in coexisting pyrrhotite and/or pyrite. Silver, Cd, and In concentrations are 0.80–51.4, 0.29–18.6, and 0.12–1.87 µg/g. Chalcopyrite consistently displays Pb concentrations above detection limits (2.10–19.3 µg/g). Much of the Sn, Sb, Te, Tl, and Bi analyses were below detection (Fig. 4).

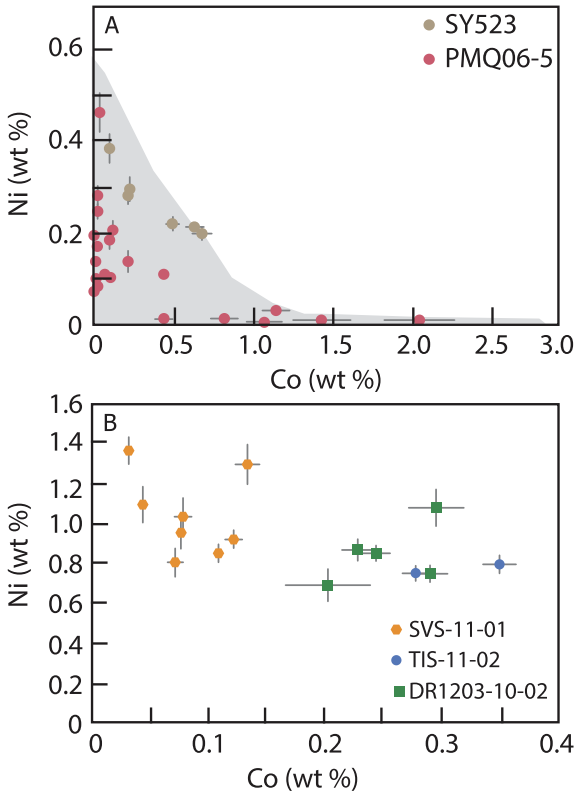

Fig. 7. Cobalt vs Ni concentrations in pyrite (A) and pyrrhotite (B). Two-sigma standard errors are given. The grey field shows the bounds of pyrite compositions for all samples, within this field only the analyses for samples for SY523 and PMQ06-5 are highlighted (A). These data show a negative correlation between Co and Ni concentrations (A). In contrast, the compilation of all pyrrhotite data (B) shows a more restricted compositional range both within and between samples.

5.2. Silicates

Garnet contains significant concentrations of Cr (≤435 μg/g), Co (3.1–63.2 μg/g), and Zn (25.1–101 μg/g), with subordinate concentrations of Ni (≤3.77 μg/g), Ga (4.00–9.54 μg/g), Ge (2.08–5.20 μg/g), In (≤0.11 μg/g), and Sn (≤0.81 μg/g). Slight intragrain variability is observed in some grains. For example, a garnet in blueschist sample DR1203-11-03 exhibits core to rim increases in Co (9.09–12.7 μg/g), Zn (25.1–33.6 μg/g), and Ga (5.39–7.16 μg/g), whereas Ge remains nearly constant. A core-to-rim increase in Co and Zn concentrations is also observed in eclogite sample G083-12 and eclogitic blackwall sample SY462. In eclogite sample TIS-11-02, Co and Zn concentrations are elevated in the mantle compared to cores and rims (*e.g.*, 100 vs 85.6–96.3 μg/g Zn), whereas in SVS-11-01, Zn decreases from core to rim (101.2 to 90.0 μg/g) and Co concentrations are unchanged.

Clinopyroxene grains were found to incorporate Cr (≤990 μg/g), Co (0.40–26.6 μg/g), Zn (19.5–129 μg/g), Ga (13.0–27.7 μg/g), and Ni (0.90–170 μg/g). Cobalt concentrations are consistently 20–30 μg/g lower in omphacite relative to coexisting garnet, whereas Ni and Zn concentrations are consistently elevated relative to garnet. Measurable concentrations of Ge (≤3.62 μg/g), In (0.053–0.18 μg/g), Sn (0.32–1.77 μg/g), and Pb (≤2.39 μg/g) are also observed. Arsenic (≤0.96 μg/g), Cd (≤0.44 μg/g), Sb (≤0.89 μg/g), and Tl (≤0.080 μg/g) are rarely above detection limits.

Analyzed amphibole grains show consistently measurable concentrations of Cr (3.70–1532 μg/g), Co (20.9–83.0 μg/g), Ni (4.88–1294 μg/g), Zn (70.3–369 μg/g), and Ga (2.73–34.9 μg/g). Germanium (≤4.30 μg/g), Cd (≤0.48 μg/g), In (≤0.64 μg/g), Sn (≤2.73 μg/g), Tl (≤0.17 μg/g), and Pb (≤2.37 μg/g) are also frequently above their detection limits. Molybdenum and Sb were only detected in one analysis each, whereas As, Ag, and Bi concentrations are below their respective detection limits in all analyses. In sample DR1203-11-03, texturally equilibrated actinolite and glaucophane are elevated in Co, Zn, and Ga relative to garnet by 20–30 μg/g, 250–300 μg/g, and 1–20 μg/g, respectively. In contrast, garnet exhibits higher Ge concentrations relative to coexisting amphibole, and Cr concentrations are roughly equivalent. Coexisting actinolite and glaucophane have similar trace element concen-

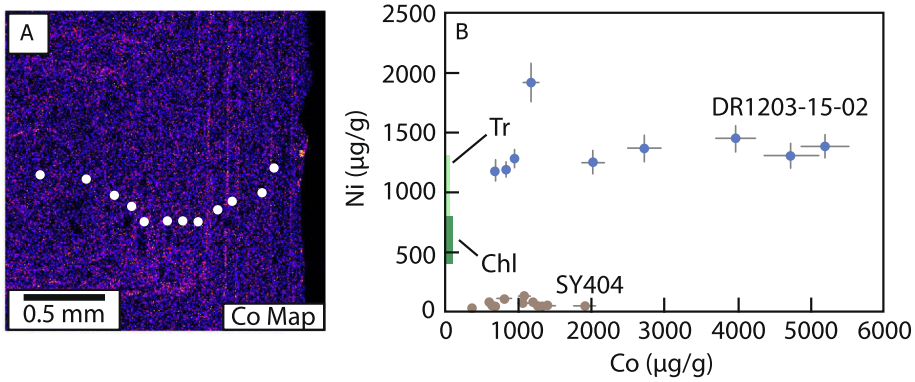

Fig. 8. Cobalt X-ray intensity map of pyrite in chlorite schist sample SY404 (A) with LA-ICP-MS analyses of Co and Ni plotted for samples SY404 and DR1203-15-02 (B). Pyrite in both samples exhibit oscillatory zoning in Co, but no observed zoning in Ni. Cobalt and Ni concentrations of coexisting chlorite ± tremolite are also shown for reference.

trations, with the exception of Ga, which is 9–12 μg/g higher in glaucophane.

White mica grains exhibit appreciable concentrations of Cr (8.40–231 μg/g), Co (2.32–36.8 μg/g), Ni (5.11–52.9 μg/g), Zn (24.9–162 μg/g), Ga (17.2–37.6 μg/g), and Tl (0.60–1.95 μg/g). White mica was found to display the highest Tl concentrations of any mineral (Fig. 6). More rarely In, Sn, Sb, and Pb are observed.

Chlorite grains were found to contain significant Cr (≤1539 μg/g), Co (0.14–71.9 μg/g), Ni (0.47–971 μg/g), Cu (≤247 μg/g), Zn (3.40–646 μg/g), and Ga (8.35–51.3 μg/g). The highest Cu concentrations were found in the blackwall Grt-Chl-Omp fels sample SY462. Similar to amphibole, elevated Cr and Ni concentrations in chlorite are observed in chlorite schist blackwall samples (DR1203-15-02, SY404). Unusually high Ni concentrations (867–971 μg/g) were also observed in retrograde chlorite associated with thiospinel in eclogite sample G083-12.

Epidote exhibits consistently measurable concentrations of Cr (5.20–444 μg/g), Co (0.28–3.11 μg/g), Zn (2.71–20.1 μg/g), Ga (41.7–146 μg/g), Ge (2.56–194 μg/g), In (0.093–1.44 μg/g), Sn (0.79–7.36 μg/g), and Pb (3.71–109 μg/g). Epidote in sample SY462 is distinct: Zn, Ga, Ge, In, and Sn are elevated relative to epidote in other samples, whereas Cr is significantly lower (Table EA5). Epidote grains in SY462 also display elevated As (17.2–26.6 μg/g) and Bi concentrations (5.73–6.64 μg/g).

Other minerals include pumpellyite, plagioclase, and titanite. Pumpellyite measured in blueschist sample DR1203-10-02 displays measurable concentrations of Cr (13.9–26.7 μg/g), Co (13.0–14.9 μg/g), Ni (19.3–28.1 μg/g), Zn (49.3–50.9 μg/g), Ga (28.7–31.6 μg/g), Ge (4.94–5.28 μg/g), and Cd (1.07–1.43 μg/g). Plagioclase exhibits only minor concentrations of Cr (≤5.20 μg/g), Ga (4.06–4.53 μg/g), and Pb (≤0.12 μg/g). Titanite was found to incorporate Cr (50.8–287 μg/g), Ni (≤3.82 μg/g), Ga (2.03–14.3 μg/g), Ge (6.02–55.1 μg/g), As (0.81–11.8 μg/g), Mo (0.36–9.60 μg/g), Cd (≤0.26 μg/g), Sn (10.3–81.6 μg/g), Sb (≤0.91 μg/g), Pb (2.03–9.67 μg/g), and Bi (0.13–0.45 μg/g).

6. DISCUSSION

6.1. Summary of observed CSE concentrations

Chalcophile and siderophile minor and trace elements in the observed samples exhibit significant intra- and inter-mineral and sample variation. Sulfides exhibit elevated Co, Ni, Cu, As, Ag, Cd, In, and Te concentrations relative to silicates (Figs. 4–6). In samples containing multiple sulfides, pyrite is elevated in Co, As, Te, and Bi, Ni is primarily hosted in pyrrhotite, and Cu, Zn, Ag, Cd, In, and Pb are contained in chalcopyrite (Fig. 4). Sulfides do not host significant concentrations of Ga, Mo, Sn, Sb, Tl, or Bi. Li et al. (2013) and Su et al. (2019) reported similar Co, Ni, Cu, Zn, As, Ag, Sb, and Bi concentrations for pyrite and chalcopyrite in eclogite and vein systems from the Tianshan (ultra-)HP metamorphic belt. However, Pb concentrations (2000–5000 μg/g) in pyrite reported by Su et al. (2019) far exceed the <10 μg/g concentrations commonly observed in our study. Additionally, Mo concentrations in chalcopyrite (0.105–236 μg/g) measured by Li et al. (2013) are 3–4 orders of magnitude higher than those measured here (<0.036 μg/g). We suggest that such elevated Pb and Mo concentrations are rare based on our global survey.

In many ore deposits, minor and trace elements may be contained in sulfide hosted nanoparticles (see review in Deditius et al., 2011). Nanoparticles containing As, Pb, Sb, Bi, Cu, Co, Ni, Zn, Au, Ag, Se, and Te have been identified, and may manifest as spikes in the downhill intensity profiles of SIMS and LA-ICP-MS analyses (*e.g.*, Pals et al., 2003; Reich et al., 2013; Román et al., 2019). Nanoparticles are most common in low-T hydrothermal deposits and are thought to form when trace metal solubility limits are reached (Deditius et al., 2011; Reich et al., 2013; Deditius and Reich, 2016;). Given that only rare Cu (±Pb) spikes are observed in pyrite grains containing chalcopyrite or galena inclusions (Fig. EA46) and concentrations of the studied elements are generally low, there is no evidence that the solubility limit was reached during cooling.

Silicate phases contain significant concentrations of Cr, Co, Ni, Zn, Ga, Mo, Cd, Sn, Tl, and Pb (Figs. 5–6). Tables 3 and 4 show a comparison of the data presented here with concentration ranges reported by in the literature (Zack et al., 2002; van der Straaten et al., 2008; El Korh et al., 2009, 2017, 2020; Spandler et al., 2011; Guo et al., 2012; Li et al., 2013, 2017; Hara et al., 2018; Su et al., 2018; Chen et al., 2019). Particularly, concentrations of Ga, Mo, Sn and Tl in silicates are elevated relative to sulfides. Cobalt, Ni, and Zn concentrations are elevated in most Fe-Mg bearing silicates, such as garnet, omphacite, and clinoamphibole (Fig. 5). Gallium concentrations are especially high in epidote (Fig. 5). Comparable Ga concentrations were also observed in lawsonite by El Korh et al. (2017) and Hara et al. (2018). Cadmium concentrations are especially high (<0.14–1.43 μg/g) in Ca-silicate minerals, particularly pumpellyite and epidote (Fig. 5J). Molybdenum and Sn are elevated in titanite relative to other silicate minerals, displaying similar concentrations to that of rutile reported in the literature (Zack et al., 2002; Li et al., 2013, 2017; Su et al., 2018; Chen et al., 2019). In contrast, Sb concentrations in titanite are lower than that of rutile reported by Zack et al. (2002). Concentrations of Tl in white mica exceed those of all other minerals by at least 1–2 orders of magnitude (Hara et al., 2018; this study), consistent with the correlations of K_2O, Rb, Cs, and Ba with Tl identified by Shu et al. (2019) from bulk rock analyses of eclogites. Lead concentrations in epidote are typically 1–2 orders of magnitude higher relative to other minerals, whereas lawsonite is the most important host of Pb at low-*T* high-*P* conditions in which epidote is not stable (*e.g.*, Hara et al., 2018; Fornash and Whitney, 2020; Whitney et al., 2020). REE-rich epidote in sample SY462 has Bi concentrations of 5.73–6.64 μg/g, consistent with the similar ionic radius of Bi^{3+} with Ce^{3+}. These data suggest that Bi partitioning may follow LREE in HP rocks.

Appreciable concentrations of Cu and As were measured in some silicate phases. Arsenic was found in epidote from sample SY462. Trivalent As has a similar ionic radius to Fe^{3+} and Al^{3+} and may substitute into the epidote structure directly. Elevated Cu contents (<0.37–247 μg/g) are

Table 3
Comparison of Cr, Co, Ni, Zn, Ga, and Ge concentrations of silicate minerals.

		Cr (μg/g)	Co (μg/g)	Ni (μg/g)	Zn (μg/g)	Ga (μg/g)	Ge (μg/g)
Grt		<2.73–435	3.08–51.9	<0.51–3.77	25.1–101	4.00–9.54	2.08–21.5
	Lit.	1.00–693	0.53–127	0.27–9.66	15.6–197.9	2.50–16.0	2.70–27.0
	$n_{Lit.}$	105	98	105	54	75	51
Cpx		2.73–990	0.88–26.6	0.90–170	19.5–129	13.0–27.7	<1.42–3.62
	Lit.	1.83–35100	0.91–86.6	4.60–629	57.0–272	8.80–40.8	1.20–2.60
	$n_{Lit.}$	294	293	294	16	18	10
Cam		3.70–1532	17.2–89.4	4.88–1294	71.5–528	2.73–34.9	<1.42–4.30
	Lit.	9.67–2061	0.358–394	9.06–1505	81.0–857	1.20–36.0	<0.10–21.0
	$n_{Lit.}$	47	41	53	39	59	32
Wm		8.00–231	2.32–36.8	8.34–52.9	24.9–162	17.2–37.6	<1.42
	Lit.	0.57–1525	3.00–27.2	6.70–415	20.0–200	26.1–188	<0.10–0.91
	$n_{Lit.}$	29	23	29	21	27	10
Chl		<2.73–1539	0.13–74.4	0.47–971	3.40–646	7.91–51.3	<1.42–3.86
	Lit.	11.0–274	139	244–649	418–1174	5.00–53.0	<0.10–4.5
	$n_{Lit.}$	5	1	5	5	17	13
Ep/Zo		5.20–444	0.24–3.11	<0.51–5.04	3.40–20.1	41.7–146	2.56–194
	Lit.	30–1541	0.19–138	1.21–28.0	8.03–46.0	20–186	2.70–19.0
	$n_{Lit.}$	40	29	33	26	116	101
Pl		<2.73–5.20	<0.057–0.69	<0.51	<0.93	4.06–4.53	<1.42
	Lit.	<3.3–17.4	1.41–1.65	<0.42–5.31	<2.60	4.00–10.0	<0.10–1.8
	$n_{Lit.}$	4	4	4	2	9	7
Ttn		50.8–259	<0.057–0.74	<0.51–3.82	<0.93–2.62	2.03–14.3	7.28–55.1
	Lit.	31.0–970	0.20–1.27	<0.42–139	5.24–271	0.41–11.0	2.1–4.2
	$n_{Lit.}$	12	2	10	10	22	14

Table 4
Comparison of As, Mo, Sn, Sb, Tl, and Pb concentrations of silicate minerals.

		As (μg/g)	Mo (μg/g)	Sn (μg/g)	Sb (μg/g)	Tl (μg/g)	Pb (μg/g)
Grt		<0.80	<0.066–0.43	<0.11–0.81	<0.26	<0.019	<0.067–0.16
	Lit.	<0.043–0.22	0.11–0.64	<0.10–0.82	<0.050–0.15	0.001–0.032	<0.050–1.07
	$n_{Lit.}$	24	10	8	50	20	54
Cpx		<0.80–0.96	<0.066	0.44–2.01	<0.26–0.89	<0.019–0.080	<0.067–2.39
	Lit.	<0.017–8.70	0.069–4.70	0.52–1.78	<0.01–2.3	0.019–0.049	0.067–21.0
	$n_{Lit.}$	56	10	143	106	6	289
Cam		<0.80	<0.066–0.091	<0.11–2.69	<0.26–0.78	<0.019–0.17	<0.067–2.37
	Lit.	<1.2–11.0	0.08–16.0	<0.10–23	1.20–20.0	0.002–0.041	0.01–39.0
	$n_{Lit.}$	4	5	4	4	20	36
Wm		<0.80	<0.066	<0.11–1.24	<0.26–0.28	0.60–1.95	<0.067–14.1
	Lit.		0.026			1.29–2.67	0.45–4.30
	$n_{Lit.}$		1			7	19
Chl		<0.80	<0.066–0.18	<0.11–1.86	<0.26–2.27	<0.019–1.06	<0.067–22.8
	Lit.		<0.23				2.71
	$n_{Lit.}$						1
Ep/Zo		<0.80–26.6	<0.066	0.79–7.36	<0.26–0.42	<0.019	3.71–109
	Lit.	13.0–22.0	<0.48–15	2.8–20.0	<0.10–16.0		5.17–279
	$n_{Lit.}$	3	10	3	3		24
Pl		<0.80	<0.066	<0.11	<0.26	<0.019	<0.067–0.12
	Lit.		<0.54				18.8–34.7
	$n_{Lit.}$		2				2
Ttn		0.81–11.8	0.36–9.60	9.14–81.6	<0.26–0.91	<0.019	2.03–9.67
	Lit.		0.21				1.25–2.16
	$n_{Lit.}$		1				4

observed in chlorite in our study. Marschall (2005) also observed high Cu concentrations (up to 3 wt.%) in chlorite associated with aegirine, hematite, and andradite in veins cutting garnet from Syros. Copper-rich chlorite (and biotite) have also been observed within the supergene zone of copper porphyry deposits for which it is suggested that Cu in chlorite occurs as metal nanoinclusions and Cu-rich expanded interlayers (*e.g.*, Ilton and Veblen, 1993). However, octahedrally-coordinated Cu^{2+} may substitute for Fe-Mg in biotite, and possibly chlorite, at high tempera-

tures and fO_2 (Hazen and Wones, 1972). Hara et al. (2018) measured concentrations up to 218 μg/g of Cu in lawsonite. Trivalent Cu may substitute for Al^{3+} if rocks are sufficiently oxidized. Monovalent Cu was the only detected species in experimental basaltic glasses equilibrated at and below the nickel-nickel oxide fO_2 buffer (Lanzirotti et al., 2019); however, the fO_2 under which Cu^{3+} may be stabilized under slab *P–T–X* conditions is unknown and further investigation is warranted.

6.2. Prograde sulfur loss and sulfide reprecipitation

Sulfides are commonly observed in HP reaction zones and veins, suggesting that significant sulfur may be mobilized during prograde subduction metamorphism (*e.g.*, Evans et al., 2014; Crossley et al., 2018; Li et al., 2020; Walters et al., 2020). Prograde sulfides in oceanic-type eclogites commonly occur as inclusions in garnet and omphacite (*e.g.*, Evans et al., 2014; Tomkins and Evans, 2015; Li et al., 2016, 2020; Walters et al., 2019; 2020; this study), whereas sulfides in textural equilibrium with the peak assemblage are rare. Studies of metapelite rocks demonstrate that sulfur may be partially conserved when pyrite is replaced by pyrrhotite during prograde regional metamorphism (*e.g.*, Tracy and Robinson, 1988). The pyrite-to-pyrrhotite reaction transfers Fe from silicate phases to produce Mg-enriched peak metamorphic silicate assemblages. Such peak eclogite facies assemblages are not observed in our samples and are not described in the literature. The thermodynamic calculations of Walters et al. (2020) instead suggest that pyrrhotite will react to form pyrite during prograde metamorphism. In the oxidized altered oceanic crust, pyrite is predicted to break down to anhydrite and release fluid-borne SO_x species over the blueschist to eclogite transition (Walters et al., 2020), whereas H_2S may form via pyrite dissolution in less altered lithologies metamorphosed at or below the quartz-fayalite-magnetite fO_2 buffer (Li et al., 2020; Walters et al., 2020). These studies predict only partial sulfur loss, with a maximum of 45% in SO_x dominant systems and lower values predicted in H_2S dominated systems.

Chalcopyrite is predicted to be replaced by an intermediate solid solution phase at pressures >1.0 GPa, which undergoes a terminal breakdown reaction to pyrite + bornite + pyrrhotite between 1.0 GPa and 1.7 GPa (Brown et al., 2020). These data are consistent with prograde inclusions of chalcocite and covellite replacing chalcopyrite in garnet in sample DR1203-11-03 (Fig. 2E), and retrograde chalcopyrite exsolution in bornite in metasediments from the Tauern Window, Austria (Walters et al., 2019) and eclogite from the Tianshan, China (Li et al., 2016). Reactions that may govern sulfur mobilization from Cu-sulfides are unclear. Regardless of the mechanism, the absence of peak metamorphic sulfides in many oceanic-type eclogite rocks and enrichment of sulfur in metasomatized HP rocks are consistent with efficient sulfur loss from subducted oceanic crust.

The samples analyzed in this study exhibit varying degrees of overprinting metasomatism and sulfide precipitation. Trace-element data of these minerals are, therefore, not representative of prograde subduction metamorphism. Eclogite samples from coherent lithotectonic units (SVS-11-01, TIS-11-02, and G083-12) display abundant retrograde amphibole grains and diopside + plagioclase symplectite (Fig. 2A–C). Pyrite grains occur with amphibole and contain inclusions of diopside and plagioclase in SVS-11-01 and TIS-11-02 (Walters et al., 2019). In all three eclogite samples, pyrite crystallized during early retrograde metamorphism is rimmed by chalcopyrite (G083-12) or chalcopyrite + pyrrhotite (SVS-11-01, TIS-11-02). The phase equilibrium models of Walters et al. (2020) show that pyrrhotite may replace pyrite during decompression and heating to granulite facies conditions, consistent with the textures observed here. Chalcopyrite associated with pyrite breakdown must have formed at ≤1.0 GPa (Brown et al., 2020), consistent with pyrite destabilization in the granulite facies.

Blackwall samples record slab-fluid induced metasomatism at peak to retrograde assemblages. For example, garnet, jadeite to aegirine clinopyroxene, and epidote are observed in sample SY462, which suggests that metasomatism and sulfide precipitation initiated under eclogite-facies conditions. Textures in other samples, such as the omphacite + pumpellyite + chalcopyrite + pyrrhotite veins (sample DR1203-10-01), albite and chalcopyrite inclusions in pyrite (sample DR1203-07-02), and pyrite overprinting the omphacite + white mica + glaucophane (blueschist sample PMQ06-5), suggest a maximum of blueschist-facies conditions. However, there are few pressure constraints for chlorite schists, which may have formed in the eclogite facies or at shallower conditions (Marschall and Schumacher, 2012).

6.3. CSE budget of the subducting oceanic crust

Here we assess the impact of sulfur loss on the Co, Ni, Zn, Ga, Ge, As, Mo, Sn, Tl, and Pb budgets for subducting mafic crust following major dehydration reactions along 'cold' and 'hot' geotherms (Fig. 9). Our sample set does not represent a suite of sulfide-bearing rocks metamorphosed at varying degrees across the blueschist-eclogite transition, and thus we prefer modeling for our budget calculations. The budgets were constructed using mineral molar fractions calculated by Hernández-Uribe and Palin (2019) in Theriak-Domino for the N-MORB composition of Gale et al. (2013). Molar fractions were calculated along the 'cold' and 'hot' geotherms from Penniston-Dorland et al. (2015). Sulfides are not included in the models of Hernández-Uribe and Palin (2019); here we assume values of 0.2 and 1.0 mol% pyrite, consistent with predicted pyrite abundances for average mid-ocean ridge basalt and altered oceanic crust metamorphosed at blueschist facies conditions (Walters et al., 2020). To assess the maximum impact of pyrite on the CSE trace-element budget, we assume complete loss of sulfides following slab dehydration. Mineral/garnet rim partition coefficients for Cr, Co, Ni, Zn, Ga, Ge, and Sn (2–4 mineral/garnet pairs) are calculated for texturally equilibrated assemblages Grt + Gln + Act + Ep + Wm + Ttn in DR1203-11-03, and Grt + Omp in G083-12, SVS-11-01, and TIS-11-02. An additional

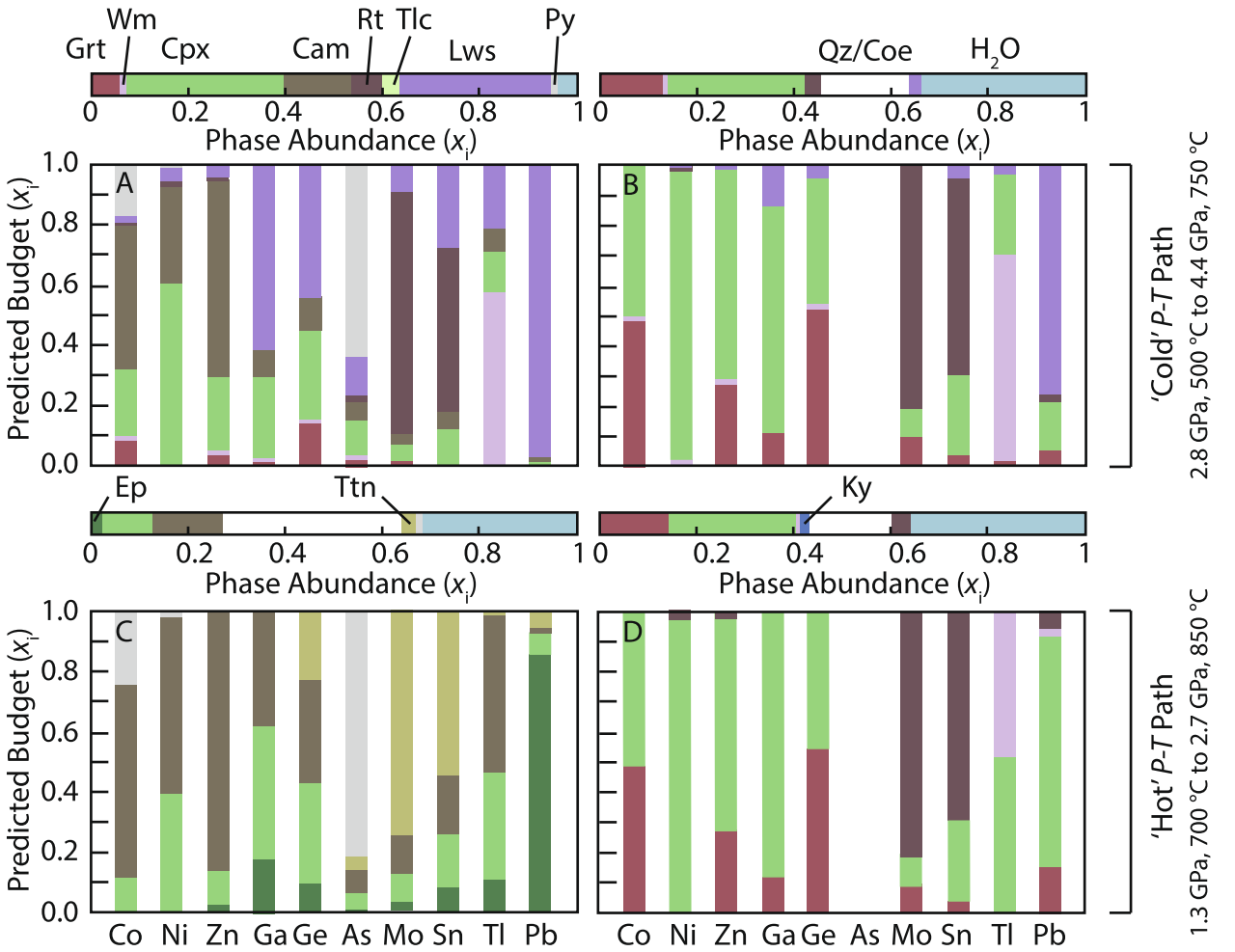

Fig. 9. Predicted trace element budgets (in mole fraction, x_i) for Co, Ni, Zn, Ga, Ge, As, Mo, Sn, and Tl at 2.8 GPa and 500 °C (A) and 4.4 GPa and 750 °C (B) along a cold subduction *P–T* path, and 1.3 GPa and 700 °C (C) and 2.7 GPa and 850 °C (D) along a warm geotherm *P–T* path. The corresponding mole fractions of the phase assemblages are shown above each *P–T* step. Calculations assume 0.2 mol% pyrite at the low *P–T* conditions (see text). Given the low abundance of As in other minerals, it is likely that As loss is complete following sulfur-loss and therefore is not included in the sulfide absent assemblage.

Brs/Grt partition coefficient was calculated for G083-12 using a barroisite inclusion paired with a nearby garnet core measurement. These data are presented in Table 5. For sulfide/garnet partition coefficients, average pyrite and garnet compositions were assumed. Matrix sulfides in eclogites retrogressed in the granulite and amphibolite facies were not formed under HP metamorphic conditions and are not included in our average. Rutile and lawsonite were not analyzed in our study, and partition coefficients were calculated from literature data. Additionally, thallium partition coefficients are calculated from the data of Hara et al. (2018), who report lower detection limits than our study. The literature data used are detailed in the Electronic Annex.

Here we find that despite high sulfide/silicate partitioning coefficients, sulfides abundances are too low (<1 vol% in most HP mafic rocks) and sulfides contribute little to the distribution of most CSE in the subducted mafic crust. Although eclogite-facies sulfide ores have been observed (*e.g.*, Giacometti et al. 2014), such rocks are rare. Instead, the CSE evolution of the slab is largely driven by the loss of hydrous phases, such as amphibole, lawsonite, and epidote. Prior to sulfide loss, pyrite hosts 18–24%, 1–2%, and >64% of the Co, Ni, and As budgets, respectively (Fig. 9). These values increase to 52–62%, 4–8%, and >90% of the Co, Ni, and As budget, respectively, if 1 mol% pyrite is assumed. Only Co and As budgets are strongly influenced by small changes in pyrite abundance. Here we find that Ni is primarily hosted by amphibole and clinopyroxene. Pyrite/garnet partition coefficients for Co and Ni are an order of magnitude higher than those of any other mineral, making the budget of these elements particularly sensitive to pyrite abundance. With a few exceptions (Fig. 4), As concentrations in silicates are below the detection limit of 0.80 μg/g. Based on this detection limit, our budget estimates the maximum permissible contribution of silicate (and oxide) phases to the As budget. These data suggest a minimum pyrite contribution of 64% of the total As budget; however, this value is likely closer to 100% in natural rocks.

Table 5
Mineral/garnet partition coefficients for Cr, Co, Ni, Zn, Ga, Ge, and Sn.

	Omp/Grt		Cam/Grt				Ep/Grt					
	Low	2SE	High	2SE	Low	2SE	High	2SE	Low	2SE	High	2SE
Cr	0.46	0.01	3.75	0.14	0.26	0.01	1.09	0.03	0.26	0.01	0.64	0.02
Co	0.42	0.01	0.64	0.02	1.7	0.05	3.26	0.18	0.02	0.05	0.02	0.06
Ni	44.1	6.5	71	32	73	33	338*					
Zn	1.25	0.07	1.41	0.06	3.648	0.23	10.03	0.79	0.08	0.02	0.11	0.02
Ga	2.46	0.12	5.05	0.39	1.068	0.085	3.90	0.28	6.54	0.44	8.09	0.53
Ge	0.36*		0.40	0.17	0.30*		0.34	0.11	0.55	0.2	0.67	0.22
Sn	3.60	1.38	7.44	4.40			11.1*				18.1*	

	Wm/Grt		Ttn/Grt					
	Low	2SE	High	2SE	Low	2SE	High	2SE
Cr	0.04	0.01	0.33	0.02	0.27	0.01	0.3	0.01
Co	0.51	0.04	0.55	0.04	0.004	0.002	0.53	0.12
Ni			10.4*				7.48*	
Zn	1.08	0.10	1.14	0.11	0.020	0.006	0.08	0.02
Ga	2.42	0.17	2.45	0.17	0.28	0.03	0.34	0.04
Ge	0.30*				1.28	0.34	1.55	0.38
Sn			1.36*				94.0*	

*Calculated relative to detection limit.

The Ga (62%) and Pb (98%) budgets are dominated by lawsonite along the cold P–T path, whereas epidote is the primary host of Pb (86%) along the hot P–T path. At 65–86% of the Zn budget, amphibole is the primary host of this element along both P–T paths. Rutile and titanite are the greatest contributors to the Mo and Sn budgets (Fig. 8). Similarly, trace abundances ($\ll$ 1 mol%) of white mica account for 60–70% of the Tl budget. Although we do not estimate budgets for Cu, Ag, Cd, and Te, these elements exhibit concentrations below detection limits in most silicate phases, consistent with charge and ionic radius constraints. It is likely that sulfides dominate the budgets for these elements.

Following dehydration and sulfide loss, the remaining CSE are distributed among garnet, omphacite, rutile, and white mica. Incomplete lawsonite breakdown is predicted to occur along the cold geotherm within the P–T limits considered here (Fig. 9) and the remaining lawsonite hosts ~75% of the Pb budget. Garnet is the primary host of Ge, whereas omphacite dominates the Ni, Zn, and Ga budgets. Cobalt is divided nearly evenly between omphacite and garnet, and Tl between white mica and omphacite. Rutile is the primary host of Mo and Sn.

In addition to budget estimates, trace element concentrations in minerals are predicted using the estimated partition coefficients and average seafloor basalt concentrations of Co, Ni, Zn, Ga, Ge, As, Mo, Sn, Tl, and Pb (see Electronic Annex). Predicted compositions assume closed system behavior during slab dehydration and are tabulated in Table EA8. Estimated mineral compositions at P–T conditions prior to significant dehydration are consistently near or within the observed range of natural compositions (Tables 3–4), whereas the excess of some elements following dehydration indicates a partial to near-total loss of these elements in natural systems.

For example, elements that almost exclusively substitute into sulfides, such as As, are likely to be almost completely expelled during sulfide breakdown. Arsenic zoning in sulfides precipitated from slab fluids (this study) and progressive As loss with metamorphic grade (Bebout et al., 1999) are consistent with significant As mobilization. Maciag and Brenan (2020) found >90% of the As to be As^{3+} in basalt melting experiments at 1200 °C and 0.1 MPa over an fO_2 range extending from 3.3 log units below to 5.3 log units above the quartz-fayalite-magnetite buffer. Therefore, some As^{3+} may be retained in apatite (Liu et al., 2017), but the P–T–X dependency of the As^{3+} to As^{5+} transition is poorly constrained. Copper, Ag, Cd, and Te are also almost exclusively hosted in sulfides and are also predicted to be expelled from the slab if sulfur loss is complete.

Cobalt, Ni, Zn, Ga, and Pb concentrations are predicted to exceed measured concentrations eclogitic minerals following dehydration, suggesting at minimum a partial loss of these elements. Consistent with our calculations, Li et al. (2013) measured prograde mass losses of 10–60% for transition metals, including Co, Ni, Cu, and Zn, in eclogite adjacent to an omphacite-rich dehydration vein. In contrast, Guo et al. (2012) determined mass gains of 2.3% and 0.5% for Co and Cu, respectively, and a mass loss of 7.5% for Ni following lawsonite-breakdown in UHP eclogite. Significant Pb loss following epidote and lawsonite breakdown is required considering the low abundance of Pb in garnet, omphacite, phengite, and rutile. These data are consistent with the experimental solid/fluid residue partition coefficients <0.10 for Pb (Kessel et al., 2005). Apatite may retain some Pb in the slab residuum but is a relatively minor phase. The studies of Chauvel et al. (1995), Kelley et al. (2005), and King et al. (2007) suggested that the loss of sulfides, which may contain Pb but are unlikely to incorporate U, from the slab may fractionate Pb from U. This

process may successively elevate the U/Pb ratio of the mantle, thereby generating the HIMU reservoir (Chauvel et al., 1995). As shown here, sulfides make a minor contribution to the Pb budget, and thus their breakdown during prograde metamorphism will not liberate significant Pb. A more likely explanation is that the solid-fluid partition coefficient of Pb is 1–2 orders of magnitude higher than that of U at *P-T* experimental conditions relatively near the epidote-out and lawsonite-out reactions (Kessel et al., 2005). Gallium, which is similarly concentrated in lawsonite and epidote, may also be lost to a significant degree during the breakdown of these minerals. While El Korh et al. (2017) did not observe any Ga loss across the blueschist to eclogite facies transition, the peak assemblage contained epidote and thus Ga is retained.

In contrast, Ge, Tl, Sn, and Mo may largely be retained in the slab. Predicted Ge concentrations at all *P–T* conditions are within or near those observed in natural garnet and omphacite (*e.g.*, El Korh et al., 2017; 2020; this study). This conclusion was also reached by El Korh et al. (2017), who found no Ge loss between blueschist- and eclogite-facies lithologies. White mica, the primary host of Tl, is stable up to 10.0 GPa (Schmidt and Poli, 2014). Therefore, the incorporation of subducted Tl into volcanic arcs may require the melting of slab-derived material, for instance in mélange diapirs, consistent with Tl isotope values of Aleutian arc magmas (Nielsen et al., 2016). Alternatively, white mica may dissolve at pressures greater than 5–6 GPa, and thus release Tl from the slab at depths beyond the arc (Schmidt and Poli, 2014). In contrast, Tl may be retained even more deeply. Thallium isotope values of ocean island basalts require a slab-derived Tl addition to the HIMU mantle component, consistent with deep Tl subduction (Blusztajn et al., 2018; Nielsen et al., 2006; Shu et al., 2019).

Predicted Mo concentrations in most minerals exceed measured concentrations for both low and high *P–T* calculations. Blueschist and eclogite Mo concentrations reported by Chen et al. (2019) are between 0.052 and 0.383 μg/g closely match the 0.05–0.53 μg/g range of altered oceanic crust measured by Freymuth et al. (2015; with the single exception of a highly altered basalt breccia with 0.95 μg/g Mo). These values are lower than the average ocean floor basalt composition of 0.662 μg/g used in our calculation, thereby explaining the discrepancy between natural and predicted Mo concentrations in HP minerals. In contrast to Mo, predicted Sn concentrations in rutile are lower than natural data (*e.g.*, Zack et al., 2002; Spandler et al., 2011; Su et al., 2018). However, Sn is likely to also be retained in eclogitic rutile and the lower concentrations likely reflect our choice of bulk composition.

Our data show that sulfides do not contribute significantly to the Mo budget of the slab. This observation is in contrast to Skora et al. (2017), who proposed that sulfides are a more important host than rutile for Mo in eclogites. The reason for this discrepancy may be the large amounts of pyrite (3.8 wt%) and pyrrhotite (2.5–3.8 wt%) added to their experiments. Instead, Ti-bearing phases such as rutile or titanite, depending on *P–T–f*O_2 conditions, are much more likely to be the most important host of Mo in most natural HP metamorphic rocks. König et al. (2008, 2010, 2011) observed slab contributions of Mo and W to volcanic arcs and varying Mo/W between arcs. Sulfides will not contribute to the fractionation of Mo from W within the slab. Instead, *f*O_2, fluid salinity, and rutile abundance are thought to be the major controls on Mo mobilization in slab fluids (Bali et al., 2012; Chen et al., 2019).

Sulfide-silicate partitioning represents the largest source of uncertainty for the budgets of Co, Ni, and As. Poor (re-) equilibration of pyrite with surrounding sulfide and silicate phases impedes the determination of exact partition coefficients. For example, linear regressions of partition coefficients for multiple chalcopyrite-pyrite, pyrrhotite-pyrite, and pyrrhotite-chalcopyrite pairs produce mean standard weighted deviations much greater than unity. This variability is observed in both sulfide replacement textures and co-precipitated sulfide pairs. Although these textures are retrograde, they suggest that trace element equilibration between pyrite and other phases may be sluggish. For example, early retrograde pyrite is partially replaced by chalcopyrite + pyr rhotite during granulite facies and amphibolite facies overprinst in samples SVS-11-01 and TIS-11-02. X-ray intensity maps and quantitative spot analyses reveal the preservation of sharp zoning in pyrite, corresponding to wt% level variations in Co, Ni, and As concentrations (*e.g.*, Fig. EA22). Consistent with these data, Brenan et al. (2000) observed no resolvable Os diffusion in pyrite in experiments conducted at 500 °C. These observations suggest that trace-element concentrations in pyrite may not reflect equilibrium with other phases. While this source of uncertainty may be great, the concentrations predicted from our mass balance calculations for Co (4000–5500 μg/g), Ni (450–850 μg/g), and As (70–90 μg/g) concentrations are well within those observed in natural rocks. Therefore, we suggest that our trace-element budgets provide a reasonable estimate for these elements. Regardless of sulfide-silicate equilibrium, the other trace elements considered in our budget, such as Zn, Ga, Mo, and Tl, exhibit negligible concentrations in sulfides, and sulfides will thus not contribute greatly to the CSE budget of the subducting mafic crust.

6.4. Cses as tracers of metasomatism

Minor and trace-element zoning in sulfides has long been utilized to investigate ore-forming processes (*e.g.*, Fleischer, 1955, Hawley and Nichol, 1961; Loftus-Hills and Solomon, 1967). Sulfide composition has been linked to changes in *P-T-X*, deformation, and kinetic and crystallographic controls (Chouinard et al., 2005; Cook et al., 2013; Peterson and Mavrogenes, 2014; Tardani et al., 2017; Román et al., 2019; Wu et al., 2019). Here we find that CSEs in sulfides from HP rocks similarly record complex *P-T-X* histories and are a useful monitor of metasomatic processes.

Pyrite from mélange blackwall samples from Syros, Dominican Republic, and Australia exhibit cyclic zoning in Co ± Ni ± As (*e.g.*, DR1203-15-02, SY404, SY523, PMQ06-5). Similar cyclic Co + Ni zoning in pyrite was also observed by Crossley et al. (2018) in chlorite and talc schist blackwall from Alpine Corsica, and such cyclic zoning is

likely characteristic of pyrite in blackwall rocks. In hydrothermal systems, Co^{2+} and Ni^{2+} form aqua- and chloro-complexes and display a transition from octahedral to tetrahedral coordination with increasing T and salinity, which occurs at lower a T for Co compared to Ni (Liu et al., 2011). This coordination change with T marks a significant increase in solubility and has been invoked to account for the lack of hydrothermal Ni deposits (Brugger et al., 2016). In contrast, Ni is fluid mobile under HP metamorphic conditions. For example, Li et al. (2013) also report a ~40% loss in Ni from lawsonite eclogite to a HP vein during prograde metamorphism. Similarly, serpentinite-derived fluids have been proposed to account for Ni addition during metasomatism observed by van der Straaten et al. (2008), Miller et al. (2009), Spandler et al. (2011), and Fornash and Whitney (2020).

Invoking such CSE enriched fluids, Evans et al. (2014) suggested that Co zoning in eclogitic sulfides may represent the passage of fluids with varying salinity. However, as shown here, the Co (and Ni) budgets of HP rocks are dominated by Fe-Mg silicates and reactions involving these phases may liberate significant Co and Ni. We demonstrate that trace-element zoning in pyrite provides a valuable record of both closed-system processes and fluid infiltration during blackwall formation.

Cobalt and Ni zoning in pyrite are negatively correlated in most metasomatized mélange samples (Fig. 6). We suggest that the observed zoning represents fluctuations between fluid- and rock-buffered conditions for various elements during metasomatism. Whether a given element is fluid- or rock-buffered depends on the concentration of that element in the fluid relative to the bulk rock and the volume of fluid reacted with the rock. Highly fluid-mobile elements, which do not substitute into most HP minerals, such as As, will reach fluid-buffered conditions even at low fluid:rock ratios, whereas elements such as Co and Ni, which are more abundant in HP minerals, will require larger degrees of fluid-rock interaction to reach fluid-buffered conditions. Below we discuss two of our sample localities as case studies illustrating how Co-Ni decoupling may be linked to variations in fluid:rock ratios.

6.4.1. Case Study I: Port Macquarie, Australia

A particularly illustrative example of Co and Ni decoupling is observed in pyrite in banded blueschist blackwall from Port Macquarie mélange in Australia. Pyrite in sample PMQ06-5 exhibits elevated Co- and As-rich (0.5–2.0 wt%) and Ni-poor (<100 μg/g) cores, whereas high Ni (200–2500 μg/g) concentrations in the rims and mantle consistently correspond to zones of lower Co concentrations (Fig. 6). Additionally, pyrite mantles and rims exhibit oscillatory Ni zoning (Fig. 2). Matrix pyrite is texturally late, occurring as large idioblastic grains that crosscut the foliation (Och et al., 2003). These textures suggest that sulfur was introduced by external fluids during retrograde metasomatism (Walters et al., 2019).

We suggest that pyrite core compositions are indicative of relatively low fluid:rock ratios. In Port Macquarie, high-grade blocks contain small lawsonite eclogite pods and layers, which are largely overprinted by banded glaucophane schists (Och et al., 2003; Tamblyn et al., 2019; 2020). The high-grade rocks experienced multiple stages of burial, metasomatism, and sulfide formation (Tamblyn et al. 2020). Elevated Co in pyrite cores may mark a local source, such as the breakdown of garnet during retrograde metamorphism, or an externally derived fluid. The sharp core-to-mantle decrease in As may have been the result of dilution as the volume of precipitated pyrite increased, or may mark the end of As-producing reactions in the mélange matrix or fluid source region. Arsenic may be sourced from the breakdown of sulfides (Bebout et al., 1999; this study) or serpentine-group minerals (Hattori et al., 2005; Ryan et al., 2019).

Elevated Ni concentrations in pyrite rims and mantles (Fig. 2) may indicate higher fluid:rock ratios. High-grade blocks at Port Macquarie are hosted within chlorite-actinolite schist and are further enclosed in unaltered serpentinite (Och et al., 2003). Mid-ocean ridge basalts exhibit an average Ni:Co ratio of ~2 (see Table EA9), similar to that of many HP mafic rocks (*e.g.*, Spandler et al., 2004; Guo et al., 2012). In contrast, HP serpentinites exhibit Ni:Co ratios of 20–25 (*e.g.*, Miller et al., 2009; Barnes et al., 2014; Cannaò et al., 2016). Given that blocks are hosted in metasomatized serpentinite, high fluid:rock ratios should be accompanied by an enrichment of Ni relative to Co in pyrite, consistent with pyrite mantle and rim compositions at Port Macquarie.

Alternative explanations for the decoupling of Ni from Co and As may be considered. One scenario is a shift in fluid sources during pyrite growth. Walters et al. (2019) found that pyrite cores in sample PMQ06-5 exhibit $\delta^{34}S$ values of −9.0 to −7.3‰, overlapping with the −8.3 to −7.7‰ range of mantle and rim analyses. While different fluid sources may have similar isotopic compositions and this explanation cannot be ruled out, there are no isotopic data supporting this scenario. In contrast, changes in fluid salinity as proposed by Evans et al. (2014) should not fractionate Co from Ni and is an unlikely alternative explanation; however, changes in Co and Ni coordination in the fluid as a function of a decrease in P-T may be possible.

6.4.2. Case Study II: Chlorite Schists

In contrast to other samples, pyrite in chlorite schist blackwalls from Syros and the Dominican Republic exhibits oscillatory zoning in Co but is unzoned in Ni (Fig. 7). These rocks, which form at the contact between high-grade mafic and metasedimentary blocks and serpentinite matrix, exhibit geochemical similarity with the serpentinite matrix (Miller et al., 2009). Consistent with the ultramafic character of chlorite schists, chlorite and actinolite in samples SY404 and DR1203-15-02 exhibit high Ni/Co ratios (Fig. 7B). In these rocks, Ni in pyrite is likely buffered by the silicate assemblage throughout the entire sulfide growth history. In contrast, high Co zones in pyrite are consistent with fluid-buffered conditions, whereas low Co zones are consistent with rock-buffered conditions for this element.

Cyclic variations in the fluid:rock ratio may be associated with pulsed fluid flow events. Rapid fluid pulses from the dehydrating slab (John et al., 2012; Taetz et al., 2018)

may drive transient increases in pore fluid pressure during released slip events at the subduction interface (see review in Gomberg, 2010). In addition to driving variations in fluid availability, fluid chemistry may also evolve in response to changes in pore pressure. For example, Peterson and Mavrogenes (2014) suggested that cyclic zoning in pyrite may record trace element saturation in ore-forming fluids as a result of instantaneous drops in pressure caused by brittle failure. They also observed significant sulfur isotopic excursions (>10‰ in $\delta^{34}S$) in pyrite associated with the trace element rich zones. These excursions are the result of fluid unmixing, which partitions the oxidized and reduced sulfur into separate brine and supercritical fluid phases, resulting in large isotopic fractionations (Drummond and Ohmoto, 1985). However, Walters et al. (2019) showed no correlation between $\delta^{34}S$ values and Co concentration in chlorite schist samples SY404 and DR1203-15-02. Viete et al. (2018) calculated pressure fluctuations of 100–350 MPa associated with oscillatory zoning in HP garnet from the Franciscan formation, CA; pressure variations of this magnitude may be too small to intersect the critical curve for subduction zone fluids (Manning, 2004). Alternatively, cyclic zoning may result from transient reaction-driven changes in porosity and permeability during metasomatism (Yardley et al., 1991).

7. CONCLUSIONS

Here we present an overview of 18 chalcophile and siderophile minor and trace elements in the subducted mafic crust and associated metasomatic lithologies. In this global survey of six exhumed terranes worldwide, we show that sulfides are the primary hosts of Cu, As, Ag, and Cd. In contrast to these five elements, the budget for other CSE is dictated by partitioning between silicate, oxide, and fluid phases:

- Fe-Mg silicates are the primary hosts of Cr, Ni, Zn, Ga, and Ge, with amphibole and omphacite making particularly large contributions to the whole-rock budget (Fig. 9).
- High concentrations of Mo and Sn are observed in titanite and are comparable to those reported for rutile (Zack et al., 2002; Li et al., 2013, 2017; Su et al., 2018; Chen et al., 2019). Additionally, sulfides make a negligible contribution to the Mo budget of subducted mafic rocks.
- Though volumetrically minor, white mica (where present) dominates the Tl budget, supporting the conclusions of Shu et al. (2019). Thallium is not hosted in sulfides in the subducted curst despite its partly chalcophile character in other settings.
- Sulfides make little contribution to the slab Pb Budget, which is dominated by epidote and lawsonite.

We suggest that sulfide breakdown or dissolution during prograde subduction metamorphism of the mafic oceanic crust (Bebout et al., 1999; Tomkins and Evans, 2015; Li et al., 2020; Walters et al., 2019; 2020) may liberate significant Cu, As, Ag, and Cd into the overlying arc-mantle wedge system. These data suggest that Cu mobilized in slab fluids will enrich some arc lavas (Noll et al., 1996; de Hoog et al., 2001; Timm et al. 2012). Although our data suggest significant Cu mobilization from the slab, more recent studies show no enrichment in Cu in arc magmas relative to MORB (Jenner et al., 2010; Lee et al., 2012; Lee and Tang 2020). We suggest three possible explanations for this conundrum: (1) Arc magmas may exhibit a largely unrecognized slab contribution of Cu, (2) These elements are filtered out in the slab-mantle interface or in the peridotitic mantle wedge, or (3) sulfur saturation is common and results in overlapping Cu concentrations between MORB and arc lavas. Therefore, the 'missing' slab signature of some CSE elements warrants further investigation.

In contrast to Cu, sulfide breakdown will not contribute greatly to Ni, Zn, Ga, and Pb loss from subducted mafic crust; instead lawsonite, epidote, and amphibole dehydration reactions are anticipated to mobilize these elements. The lack of a sulfide contribution to the Pb budget is particularly important, as this means that sulfides are not responsible for the fractionation of Pb from U in the slab and will not help to solve the 'Pb paradox' (*e.g.*, Chauvel et al., 1995. The elements Ge, Tl, and Sn + Mo may be retained in the slab in garnet, white mica, and rutile, respectively. Copper and Mo are typically enriched in arc-related ore deposits (see review by Richards, 2011), but would be decoupled by prograde sulfur loss to slab fluids. Molybdenum enrichment in these deposits may require slab melting, mélange melting or other process. Alternatively, the cycling of Ge, Tl, Sn, and Mo into the overlying arc-mantle wedge system may require slab fluxing by external fluids, mélange or slab melting, or dehydration at elevated fO_2 conditions (*e.g.*, Nielsen et al., 2016; Chen et al., 2019).

We also demonstrate that CSE zoning in sulfides and silicates may be used to track metasomatism in HP rocks. In subduction mélanges, zoning of Co and Ni in pyrite reaction or 'blackwall' zones on mafic blocks record variations in the degree of fluid buffering during sulfide growth. Fluid buffering conditions are reached at different stages for Co and Ni as a function of fluid:rock ratio and bulk composition, thereby decoupling these geochemically rather similar elements. We also suggest that oscillatory zoning of some mélange blackwall pyrite grains records cyclic changes in fluid abundance, consistent with seismicity- or reaction-induced porosity changes.

Declaration of Competing Interest

The authors declare that they have no known competing financial interests or personal relationships that could have appeared to influence the work reported in this paper.

ACKNOWLEDGEMENTS

JBW acknowledges Fulbright and Chase Distinguished Research Fellowships. This work was supported by NSF grant EAR1725301 awarded to AMC. We would like to thank Martin Yates and Heidi Höfer for assistance with EPMA analyses, David Hernández-Uribe for providing the molar phase abundances from Hernández-Uribe &

Palin (2019), and Christopher McFarlane for analytical advice. Andrew Tomkins, Afifé El Korh, and an anonymous reviewer are thanked for their insightful and constructive comments. We also thank Associated Editor Martin Reich for excellent handling of this manuscript.

RESEARCH DATA FOR THIS ARTICLE

Additional data are provided in the Electronic Annex. The annex contains spreadsheets with major and minor element compositional data (Tables EA1–EA2), external reproducibility on secondary reference materials (Table EA3), minor and trace element compositional data (Tables EA4–EA5), LA-ICP-MS internal standard element values (Table EA6), average limits of detection (Table EA7), mineral trace element compositions predicted by our mass balance constraints (Table EA8), and average basalt trace element compositions used in our mass balance calculations (Table EA9). Additional figures include sulfide X-ray intensity maps with plotted compositions (Figs. EA1–EA22), garnet X-ray intensity maps (Figs. E A23–EA26), a comparison of LA-ICP-MS and EPMA data for pyrite (Fig. EA27), sulfide and garnet EPMA transects (Figs. EA27–EA30), an amphibole classification diagram Fig. (EA31), LA-ICP-MS analysis locations (Figs. EA32–EA43), amphibole trace element compositions for DR1203-10-02 (Fig. EA44), a plot of Sn vs In from epidote analyses (Fig. EA45), and an example of time resolved pyrite LA-ICP-MS spectra (Fig. EA46). Additional methods and descriptions of calculations may be found in the electronic annex.

APPENDIX A. SUPPLEMENTARY MATERIAL

Supplementary data to this article can be found online at https://doi.org/10.1016/j.gca.2021.04.016.

REFERENCES

Aulbach S., Stachel T., Seitz H. M. and Brey G. P. (2012) Chalcophile and siderophile elements in sulphide inclusions in eclogitic diamonds and metal cycling in a Paleoproterozoic subduction zone. *Geochim. Cosmochim. Acta* **93**, 278–299.

Bali E., Keppler H. and Audetat A. (2012) The mobility of W and Mo in subduction zone fluids and the Mo-W-Th-U systematics of island arc magmas. *Earth Planet. Sci. Lett.* **351–352**, 195–207.

Barnes J. D., Beltrando M., Lee C. T. A., Cisneros M., Loewy S. and Chin E. (2014) Geochemistry of alpine serpentinites from rifting to subduction: A view across paleogeographic domains and metamorphic grade. *Chem. Geol.* **389**, 29–47.

Bebout G. E., Ryan J. G., Leeman W. P. and Bebout A. E. (1999) Fractionation of trace elements by subduction-zone metamorphism — effect of convergent-margin thermal evolution. *Earth Planet. Sci. Lett.* **171**, 63–81.

Blusztajn J., Nielsen S. G., Marschall H. R., Shu Y., Ostrander C. M. and Hanyu T. (2018) Thallium isotope systematic in volcanic rocks from St. Helena – Constraints on the origin of the HIMU reservoir. *Chem. Geol.* **476**, 292–301.

Brandelik A. and Massonne H. J. (2004) PTGIBBS-an Excell™ Visual Basic program for computing and visualizing thermodynamic functions and equilibria of rock-forming minerals. *Comp. Geosci.* **30**, 909–923.

Breeding C. M., Ague J. J. and Bröcker M. (2004) Fluid-metasedimentary rock interactions in subduction-zone mélange: Implications for the chemical composition of arc magmas. *Geology* **32**, 1041–1044.

Brenan J. M., Cherniak D. J. and Rose L. A. (2000) Diffusion of osmium in pyrrhotite and pyrite: Implications for closure of the Re-Os isotopic system. *Earth Planet. Sci. Lett.* **180**, 399–413.

Brown J. L., Dyer S. C., Mungall J. E., Christy A. G. and Ellis D. J. (2020) High-pressure Cu-Fe-S phase equilibria: Some experimental and thermodynamic constraints on sulfides in subduction zones and the lithospheric mantle. *J. Petrol.* **61**, 1–16.

Brugger J., Liu W., Etschmann B., Mei Y., Sherman D. M. and Testemale D. (2016) A review of the coordination chemistry of hydrothermal systems, or do coordination changes make ore deposits?. *Chem. Geol.* **447**, 219–253.

Cannaò E., Scambelluri M., Agostini S., Tonarini S. and Godard M. (2016) Linking serpentinite geochemistry with tectonic evolution at the subduction plate-interface: The Voltri Massif case study (Ligurian western Alps, Italy). *Geochim. Cosmochim. Acta* **190**, 115–133.

Chauvel C., Goldstein S. L. and Hofmann A. W. (1995) Hydration and dehydration of oceanic crust controls Pb evolution in the mantle. *Chem. Geol.* **126**, 65–75.

Chen S., Hin R. C., John T., Brooker R., Bryan B., Niu Y. and Elliott T. (2019) Molybdenum systematics of subducted crust record reactive fluid flow from underlying slab serpentine dehydration. *Nat. Comm.* **10**, 4773.

Collett S., Štípská P., Schulmann K., Peřestý V., Soldner J., Anczkiewicz R., Lexa O. and Kylander-Clark A. (2018) Combined Lu-Hf and Sm-Nd geochronology of the Mariánské Lázně Complex: New constraints on the timing of eclogite- and granulite-facies metamorphism. *Lithos* **304–307**, 74–94.

Cook N. J., Ciobanu C. L., Meria D., Silcock D. and Wade B. (2013) Arsenopyrite-pyrite association in an orogenic gold ore: Tracing mineralization history from textures and trace elements. *Econ. Geol.* **108**, 1273–1283.

Crossley R. J., Evans K. A., Jeon H. and Kilburn M. R. (2018) Insights into sulfur cycling in subduction zones from in-situ isotope analysis of sulphides in high-pressure serpentinites and 'hybrid' samples from Alpine Corsica. *Chem. Geol.* **493**, 359–378.

Chouinard A., Paquette J. and Williams-Jones A. E. (2005) Crystallographic controls on trace-element incorporation in auriferous pyrite from the Pascua epithermal high-sulfidation deposit, Chile-Argentina. *Canadian Mineral* **43**, 951–963.

Cruz-Uribe A. M., Marschall H. R., Gaetani G. A. and Le Roux V. (2018) Generation of alkaline magmas in subduction zones by partial melting of mélange diapirs – An experimental study. *Geology* **46**, 343–346.

Dale C. W., Burton K. W., Pearson D. G., Gannoun A., Alard O., Argles T. W. and Parkinson I. J. (2009) Highly siderophile element behaviour accompanying subduction of oceanic crust: Whole rock and mineral-scale insights from a high-pressure terrain. *Geochim. Cosmochim. Acta* **73**, 1394–1416.

Deditius A. and Reich M. (2016) Constraints on the solid solubility of Hg, Tl, and Cd in arsenian pyrite. *Am. Mineral.* **101**, 1451–1459.

Deditius A., Utsunomiya S., Reich M., Kesler S. E., Ewing R. C., Hough R. and Walshe J. (2011) Trace metal nanoparticles in pyrite. *Ore Geol. Rev.* **42**, 32–46.

de Hoog J. C. M., Mason P. R. D. and van Bergen M. J. (2001) Sulfur and chalcophile elements in subduction zones: Constraints from a laser ablation ICP-MS study of melt inclusions from Galunggung Volcano, Indonesia. *Geochim. Cosmochim. Acta* **65**, 3147–3164.

Drummond S. E. and Ohmoto H. (1985) Chemical evolution and mineral deposition in boiling hydrothermal systems. *Econ. Geol.* **80**, 126–147.

Ellam R. M. and Hawksworth C. J. (1988) Elemental and isotopic variations in subduction related basalts: Evidence for a three component model. *Contrib. Mineral. Pet.* **98**, 72–80.

El Korh A., Schmidt S. T., Ulianov A. and Potel S. (2009) Trace element partitioning in HP-LT metamorphic assemblages during subduction-related metamorphism, Ile de Groix, France: A detailed LA-ICPMS study. *J. Petrol.* **50**, 1107–1148.

El Korh A., Luais B., Boiron M.-C., Deloule E. and Cividini D. (2017) Investigation of Ge and Ga exchange behaviour and Ge isotopic fractionation during subduction zone metamorphism. *Chem. Geol.* **449**, 165–181.

El Korh A., Boiron M.-C., Cathelineau M., Deloule E. and Luais B. (2020) Tracing metallic pre-concentrations in the Limousin ophiolite-derived rocks and Variscan granites (French Massif Central). *Lithos* **356–357** 105345.

Escuder-Viruete J. and Pérez-Estaún A. (2013) Contrasting exhumation P-T paths followed by high-P rocks in the northern Caribbean subduction-accretionary complex: Insights from the structural geology, microtextures, and equilibrium assemblage diagrams. *Lithos* **160–161**, 117–144.

Escuder-Viruete J., Valderde-Vaquero P., Rojas-Agramonte Y., Gabites J., Castillo-Carrión M. and Pérez-Estaún A. (2013) Timing and deformational events in the Rio San Juan complex: Implications for the tectonic controls on the exhumation of high-P rocks in the northern Caribbean subduction-accretionary prism. *Lithos* **177**, 416–435.

Evans K. A., Tomkins A. G., Cliff J. and Fiorentini M. L. (2014) Insights into subduction zone sulfur recycling from isotopic analysis of eclogite-hosted sulfides. *Chem. Geol.* **365**, 1–19.

Faryad S. W., Perraki M. and Vrána S. (2006) P-T evolution and reaction textures in retrogressed eclogites from Svetlik, the Moldanubian Zone (Czech Republic). *Mineral. Pet.* **88**, 297–319.

Faryad S. W., Jedlicka R. and Collett S. (2013) Eclogite facies rocks of the Monotonous unit, clue to Variscan suture in the Moldanubian Zone (Bohemian Massif). *Lithos* **179**, 353–363.

Fleischer M. (1955) Minor elements in some sulfide minerals. In *Economic Geology Fiftieth Anniversary Volume 1905–1955, Part II* (ed. A. M. Bateman). Econ. Geol. Pub. Co., Urbana, Ill, pp. 97–1024.

Fornash K. and Whitney D. (2020) Lawsonite-rich layers as records of fluid and element mobility in subducted crust (Sivrihisar Massif, Turkey). *Chem. Geol.* **533** 119356.

Freymuth H., Vils F., Willbold M., Taylor R. N. and Elliot T. (2015) Molybdenum mobility and isotopic fractionation during subduction at the Mariana arc. *Earth Plan. Sci. Lett.* **432**, 176–186.

Gale A., Dalton C. A., Langmuir C. H., Su Y. and Shilling J. G. (2013) The mean composition of ocean ridge basalts. *Geochem., Geophys. Geosys.* **14**, 489–518.

George L. L., Biagioni C., D'Orazio M. and Cook N. J. (2018) Textural and trace element evolution of pyrite during greenschist facies metamorphic recrystallization in the southern Apuan Alps (Tuscany, Italy): Influence on the formation of Tl-rich sulfosalt melt. *Ore Geol. Rev.* **102**, 59–105.

Giacometti F., Evans K. A., Rebay G., Cliff J., Tomkins A. G., Rossetti P., Vaggelli G. and Adams D. T. (2014) Sulfur isotope evolution in sulfide ores from Western Alps: Assessing the influence of subduction-related metamorphism. *Geochem. Geophys. Geosys.* **15**, 3808–3829.

Godard G. (2009) Two orogenic cycles recorded in eclogite-facies gneiss from the southern Armorican Massif (France). *Eur. J. Min.* **21**, 1173–1190.

Gomberg J. (2010) Slow-slip phenomena in Cascadia from 2007 and beyond: A review. *Geol. Soc. Am. Bull.* **122**, 963–978.

Guo S., Ye K., Chen Y., Liu J., Mao Q. and Ma Y. (2012) Fluid-rock interaction and element mobilization in UHP metabasalt: Constraints from an omphacite-epidote vein and host eclogites in the Dabie orogen. *Lithos* **136**, 145–167.

Hara T., Tsujimori T., Chang Q. and Kimura J. I. (2018) *In-situ* Sr-Pb isotope geochemistry of lawsonite: A new method to investigate slab-fluids. *Lithos* **320–321**, 93–104.

Hattori K., Takahashi Y., Guillot S. and Johanson B. (2005) Occurrence of arsenic (V) in forearc mantle serpentinites based on X-ray absorption spectroscopy study. *Geochim. Cosmochim. Acta* **69**, 5585–5596.

Hawley J. E. and Nichol I. (1961) Trace elements in pyrite and chalcopyrite of different ores. *Econ. Geol.* **56**, 467–487.

Hawthorne F. C., Oberti R., Harlow G. E., Maresch W. V., Martin R. F., Schumacher J. C. and Welch M. D. (2012) Nomenclature of the amphibole supergroup. *Am. Mineral.* **97**, 2031–2048.

Hazen R. M. and Wones D. R. (1972) The effect of cation substitutions on the physical properties of tri-octahedral micas. *Am. Mineral.* **57**, 103–129.

Hernández-Uribe D. and Palin R. M. (2019) A revised petrological model for subducted oceanic crust: Insights from phase equilibrium modelling. *J. Met. Geol.* **37**, 745–768.

Ilton E. and Veblen D. (1993) Origin and mode of copper enrichment in biotite from rocks associated with porphyry copper deposits: A transmission electron microscopy investigation. *Econ. Geol.* **88**, 885–900.

Jelínek E., Štědrá V. and Cháb J. (1997) The Mariánské Lázně Complex. In *Geological model of western Bohemia related to the KTB borehole in Germany* (eds. S. Vrana and V. Štědrá). Czech Geol. Survey, Prague, pp. 61–70.

Jenner F., O'Neill H. S. C., Arculus R. J. and Mavrogenes J. A. (2010) The magnetite crisis in the evolution of arc-related magmas and the initial concentration of Au, Ag and Cu. *J. Petrol.* **51**, 2445–2464.

Jochum K. P., Weis U., Stoll B., Kuzmin D., Yang Q., Raczek I., Jacob D. E., Stracke A., Birbaum K., Frick D. A., Günther D. and Enzwiler J. (2011) Determination of reference values for NIST SRM 610–617 glasses following ISO guidelines. *Geostand. Geoanalyt. Res.* **35**, 397–429.

John T., Gussone N., Podladchikov Y. Y., Bebout G. E., Dohmen R., Halama R., Klemd R., Magna T. and Seitz H. M. (2012) Volcanic arcs fed by rapid pulsed fluid flow through subducting slabs. *Nat. Geosci.* **5**, 489–492.

Kelley K., Plank T., Farr L., Ludden J. and Staudigel H. (2005) Subduction cycling of U, Th, and Pb. *Earth Plan. Sci. Lett.* **234**, 369–383.

Kepezhinskas P., Defant M. J. and Widom E. (2002) Abundance and distribution of PGE and Au in the island-arc mantle: Implications for sub-arc metasomatism. *Lithos* **60**, 113–128.

Kessel R., Schmidt M. W., Ulmer P. and Pettke T. (2005) Trace element signature of subduction-zone fluids, melts and supercritical liquids at 120–180 km depth. *Nature* **437**, 724–727.

King R. L., Bebout G. E., Grove M., Moriguti T. and Nakamura E. (2007) Boron and lead isotope signatures of subduction-zone mélange formation: Hybridization and fractionation along the slab-mantle interface beneath volcanic arcs. *Chem. Geol.* **239**, 305–322.

Kogiso T., Tatsumi Y. and Nakano S. (1997) Trace element transport during dehydration processes in the subducted oceanic crust: 1. Experiments and implications for the origin of ocean island basalts. *Earth Planet. Sci. Lett.* **148**, 193–205.

König S., Münker C., Schuth S. and Garbe-Schönberg D. (2008) The geochemical behavior of Sb, Mo and W in subduction zones. *Geochim. Cosmochim. Acta* **72**, A488.

König S., Münker C., Schuth S., Luguet A., Hoffman J. E. and Kuduon J. (2010) Boninites as windows into trace element mobility in subduction zones. *Geochim. Cosmochim. Acta* **74**, 684–704.

König S., Münker C., Hohl S., Paulick H., Barth A. R., Lagos M., Pfänder J. and Büchl A. (2011) The Earth's tungsten budget during mantle melting and crust formation. *Geochim. Cosmochim. Acta* **75**, 2119–2136.

Krebs M., Maresch W. V., Schertle H.-P., Baumann A., Draper G., Idlemann B., Münker C. and Trapp E. (2008) The dynamics of intra-oceanic subduction zones: a direct comparison between fossil petrological evidence (Rio San Juan Complex, Dominican Republic) and numerical simulation. *Lithos* **103**, 106–137.

Krebs M., Schertle H.-P., Maresch W. V. and Draper G. (2011) Mass flow in serpentinite-hosted subduction channels: P-T-t path patterns of metamorphic blocks in the Rio San Juan mélange (Dominican Republic). *J. Asian Earth Sci.* **42**, 569–595.

Lanzirotti A., Lopaka L., Head E., Sutton S. R., Newville M., McCanta M., Lerner A. and Wallace P. J. (2019) Direct measurements of copper speciation in basaltic glasses: Understanding the relative roles of sulfur and oxygen in copper complexation in melts. *Geochim. Cosmochim. Acta* **267**, 164–178.

Laurent V., Lanari P., Naïr I., Augier R., Lahfid A. and Jolivet L. (2018) Exhumation of eclogite and blueschists (Cyclades, Greece): Pressure-temperature evolution determined by thermobarometry and garnet equilibrium modelling. *J. Met. Geol.* **36**, 769–798.

Leake B. E., Woolley A. R., Arps C. E. S., Birch W. D., Gilbert M. C., Grice J. D., Hawthorne F. C., Kato A., Kisch H. J., Krivovichev V. G., Linthout K., Laird J., Mandarino J. A., Maresch W. V., Nickel E. H., Rock N. M. S. and Schumacher J. C. (1997) Nomenclature of the amphibole: Report of the subcommittee on amphiboles of the International Mineralogical Association, Commission on New Minerals and Mineral Names. *Canadian Mineral.* **35**, 219–246.

Lee C.-T. A., Luffi P., Chin E. J., Bouchet R., Dasgupta R., Morton D. M., Le Roux V., Yin Q.-Z. and Jin D. (2012) Copper systematics in arc magmas and implications for crust-mantle differentiation. *Science* **336**, 64–68.

Lee C.-T. A. and Tang M. (2020) How to make porphyry copper deposits. *Earth Planet. Sci. Lett.* **529** 115868.

Li J. L., Gao J., John T., Klemd R. and Su W. (2013) Fluid-mediated metal transport in subduction zones and its link to arc-related giant ore deposits: Constraints from a sulfide-bearing HP vein in lawsonite eclogite (Tianshan, China). *Geochim. Cosmochim. Acta* **120**, 326–362.

Li J. L., Gao J., Klemd R., John T. and Wang X. S. (2016) Redox processes in subducting oceanic crust recorded by sulfide-bearing high-pressure rocks and veins (SW Tianshan, China). *Contrib. Mineral. Pet.* **171**(72), 1–24.

Li J. L., John T., Gao J., Klemd R. and Wang X. S. (2017) Subduction channel fluid-rock interaction and mass transfer: Constraints from a retrograde vein in blueschist (SW Tianshan, China). *Chem. Geol.* **456**, 28–42.

Li J. L., Schwarzenbach E. M., John T., Ague J. J., Huang F., Gao J., Klemd R., Whitehouse M. J. and Wang X. S. (2020) Uncovering and quantifying the subduction zone sulfur cycle from the slab perspective. *Nat. Comm.* **11**, 514.

Liu W., Borg S. J., Testemale D., Etschmann B., Hazemann J. L. and Brugger J. (2011) Speciation and thermodynamic properties for cobalt chloride complexes in hydrothermal fluids at 35-440°C and 600 bar: An in-situ XAS study. *Geochim. Cosmochim. Acta* **75**, 1227–1248.

Liu W., Mei Y., Etschmann B., Brugger J., Pearce M., Ryan C. G., Borg S., Wykes J., Kappen P., Paterson D., Boesenberg U., Garrevoet J., Moorhead G. and Falkenberg G. (2017) Arsenic in hydrothermal apatite: Oxidation state, mechanism of update, and comparison between experiments and nature. *Geochim. Cosmochim. Acta* **196**, 144–159.

Loftus-Hills G. and Solomon M. (1967) Cobalt, nickel and selenium in sulphides as indicators of ore genesis. *Miner. Dep.* **2**, 228–242.

Lorand J.-P. and Luguet A. (2015) Chalcophile and siderophile elements in mantle rocks: Trace elements controlled by trace minerals. *Rev. Min. Geochem.* **81**, 441–488.

Luguet A., Lorand J.-P. and Seyler M. (2003) Sulfide petrology and highly siderophile element geochemistry of abyssal peridotites: A coupled study of samples from the Kane Fracture Zone (45° W 23°20N, MARK area, Atlantic Ocean). *Geochim. Cosmochim. Acta* **67**, 1553–1570.

Maciag B. J. and Brenan J. M. (2020) Speciation of arsenic and antimony in basaltic magmas. *Geochim. Cosmochim. Acta* **276**, 198–218.

Manning C. E. (2004) The chemistry of subduction-zone fluids. *Earth and Planet. Sci. Lett.* **223**, 1–16.

Marschall H. R. (2005) *Lithium, beryllium and boron in high-pressure metamorphic rocks from Syros (Greece)*. Universität Heidelberg, Heidelberg.

Marschall H. R., Ludwig T., Altherr R., Kalt A. and Tonarini S. (2006) Syros metasomatic tourmaline: Evidence for very high-δ^{11}B fluids in subduction zones. *J. Petrol.* **47**, 1915–1942.

Marschall H. R. and Schumacher J. C. (2012) Arc magmas sourced from mélange diapirs in subduction zones. *Nat. Geosci.* **12**, 862–867.

McInnes B., McBride J. S., Evans N. J., Lambert D. D. and Andrew A. S. (1999) Osmium isotope constraints on ore metal recycling in subduction zones. *Science* **286**, 512–516.

Miller D. P., Marschall H. R. and Schumacher J. C. (2009) Metasomatic formation and petrology of blueschist-facies hybrid rocks from Syros (Greece): Implications for reactions at the slab-mantle interface. *Lithos* **107**, 53–67.

Nielsen S. G., Rehkämper M., Norman M. D., Halliday A. N. and Harrison D. (2006) Thallium isotopic evidence for the ferromanganese sediments in the mantle source of Hawaiian basalts. *Nature* **439**, 314–317.

Nielsen S. G., Yogodzinski G., Prytulak J., Plank T., Kay S. M., Kay R. W., Blusztajn J., Owens J. D., Auro M. and Kading T. (2016) Tracking along-arc sediment inputs to the Aleutian arc using thallium isotopes. *Geochim. Cosmochim. Acta* **181**, 217–237.

Noll P. D., Newsom H. E., Leeman W. P. and Ryan J. G. (1996) The role of hydrothermal fluids in the production of subduction zone magmas: Evidence from siderophile and chalcophile trace elements and boron. *Geochim. Cosmochim. Acta* **60**, 587–611.

Nutman A., Buckman S., Hidaka H., Kamiichi T. and Belousova E. (2013) Middle Carboniferous-Early Triassic eclogite-blueschist blocks within a serpentinite mélange at Port Macquarie, eastern Australia: Implications for the evolution of Gondwana's eastern margin. *Gondwana Res.* **24**, 1038–1050.

O'Brien P. J. (1997) Garnet zoning and reaction textures in overprinted eclogites, Bohemian Massif, European Variscides: A record of their thermal history during exhumation. *Lithos* **41**, 119–133.

O'Brien P. J. and Vrána S. (1995) Eclogites with a short-lived granulite facies overprint in the Moldanubian Zone, Czech Republic: petrology, geochemistry and diffusion modeling of garnet zoning. *Geolog. Runds.* **84**, 473–488.

Och D. J., Leitch E. C., Caprarelli G. and Watanabe T. (2003) Blueschist and eclogite in tectonic mélange, Port Macquarie, New South Wales. *Australia. Mineral. Mag.* **67**, 609–624.

Pals D. W., Spry P. G. and Chryssoulis S. (2003) Invisible gold and tellurium in arsenic-rich pyrite from the Emperor gold deposit, Fiji: Implications for gold distribution and deposition. *Econ. Geol.* **98**, 479–493.

Paton C., Hellstrom J., Paul B., Woodhead J. and Hergt J. (2011) Iolite: Freeware for the visualization and processing of mass spectrometric data. *J. Analyt. Atom. Spect.* **26**, 2508–2518.

Patten C. G. C., Pitcairn I. K., Teagle D. A. H. and Harris M. (2016a) Mobility of Au and related elements during the hydrothermal alteration of the oceanic crust: Implications for the sources of metals in VMS deposits. *Mineral. Dep.* **51**, 179–200.

Patten C. G. C., Pitcairn I. K., Teagle D. A. H. and Harris M. (2016b) Sulphide mineral evolution and metal mobility during alteration of the oceanic crust: Insights from ODP Hole 1256D. *Geochim. Cosmochim. Acta* **193**, 132–159.

Pearce N. J. G., Perkins W. T., Westgate J. A., Gorton M. P., Jackson S. E., Neal C. R. and Chenery S. P. (1997) A compilation of new and published major and trace element data for NIST SRM 610 and NIST SRM 612 glass reference materials. *Geostand. Newslett.* **21**, 115–144.

Penniston-Dorland S. C., Kohn M. J. and Manning C. E. (2015) The global range of subduction zone thermal structures from exhumed blueschists and eclogites: Rocks are hotter than models. *Earth Planet. Sci. Lett.* **428**, 243–254.

Peterson E. and Mavrogenes J. (2014) Linking high-grade gold mineralization to earthquake-induced fault-valve processes in the Porgera gold deposit, Papua New Guinea. *Geology* **42**, 383–386.

Peucat J. J., Vidal P., Godard G. and Postaire B. (1982) Precambrian U-Pb zircon ages in eclogites and garnet pyroxenites from South-Brittany (France): An old oceanic crust in the West European Hercynian belt? *Earth Planet Sci. Lett.* **60**, 70–78.

Plank T. and Langmuir C. H. (1993) Tracing trace elements from sediment input to volcanic output at subduction zones. *Nature* **362**, 739–742.

Reich M., Deditius A., Chryssoulis S., Li J. W., Ma C. Q., Parada M. A., Barra F. and Mittermayr F. (2013) Pyrite as a record of hydrothermal fluid evolution in a porphyry copper system: A SIMS/EPMA trace element study. *Geochim. Cosmochim. Acta* **104**, 42–62.

Richards J. P. (2011) Magmatic to hydrothermal metal fluxes in convergent and collided margins. *Ore Geol. Rev.* **40**, 1–26.

Román N., Reich M., Leisen M., Morata D., Barra F. and Deditius A. P. (2019) Geochemical and micro-textural fingerprints of boiling in pyrite. *Geochim. Cosmochim. Acta* **246**, 60–85.

Ryan P. C., Huertas F. J., Pincus L. N. and Painter W. (2019) Arsenic-bearing serpentine-group minerals: Mineral synthesis with insights for the arsenic cycle. *Clays Clay Min.* **67**, 488–506.

Schertl H.-P., Maresch W. V., Stanek K. P., Hertwig A., Krebs M., Baese M. and Sergeev S. S. (2012) New occurences of jadeitite, jadeite quartzite and jadeite-lawsonite quartzite in the Dominican Republic, Hispaniola: Petrological and geochronological overview. *Eur. J. Mineral.* **24**, 199–216.

Schmidt M. W. and Poli S. (2014) Devolatilization during subduction. In *Treatise on Geochemistry* (eds. H. D. Holland and K. K. Turekian). Elsevier, Amsterdam, pp. 669–701.

Schumacher J. C. (1991) Empirical ferric iron corrections: Necessity, assumptions, and effects on selected geobarometers. *Min. Mag.* **55**, 3–18.

Shu Y., Nielsen S., Marschall H. R., John T., Blusztajn J. and Auro M. (2019) Closing the loop: Subducted eclogites match thallium isotope compositions of ocean island basalts. *Geochim. Cosmochim. Acta* **250**, 130–148.

Sillitoe R. H. (1972) Relation of metal provinces in western America to subduction of oceanic lithosphere. *Geol. Soc. Am. Bull.* **83**, 813–818.

Skora S., Freymuth H., Blundy J., Elliot T. and Guillong M. (2017) An experimental study of the behavior of cerium/molybdenum ratios during subduction: Implications for tracing the slab component in the Lesser Antilles and Mariana Arc. *Geochim. Cosmochim. Acta* **212**, 133–155.

Spandler C., Hermann J., Arculus R. and Mavrogenes J. (2004) Geochemical heterogeneity and elemental mobility in deeply subducted oceanic crust: Insights from high-pressure mafic rocks from New Caledonia. *Chem. Geol.* **206**, 21–42.

Spandler C., Pettke T. and Rubatto D. (2011) Internal and external fluid sources for eclogite-facies veins in the Monviso metaophiolite, western Alps: Implications for fluid flow in subduction zones. *J. Pet.* **52**, 1207–1236.

Spandler C. and Pirard C. (2013) Element recycling from subducting slabs to arc crust: A review. *Lithos* **170–171**, 208–223.

Štědrá V. (2001) *Tectonometamorphic evolution of the Mariánské Lázně Complex, Western Bohemia, based on the study of metabasic rocks*. Charles University, Prague.

Stolper E. and Newman S. (1994) The role of water in petrogenesis of Marian trough magmas. *Earth Planet. Sci. Lett.* **121**, 293–325.

Su W., Li J. L., Mao Q., Gao J., Liu X., Chen F. and Ge X.-M. (2018) Rutile in HP rocks from the western Tianshan, China: Mineralogy and its economic implications. *J. Earth Sci.* **29**, 1049–1059.

Su W., Schwarzenbach E. M., Chen L., Li Y., John T., Gao J., Chen F. and Hu X. (2019) Sulfur isotope compositions of pyrite from high-pressure metamorphic rocks and related veins (SW Tianshan, China): Implications for the sulfur cycle in subduction zones. *Lithos* **348–349** 105212.

Tamblyn R., Hand M., Kelsey D., Anczkiewicz R. and Och D. (2019) Subduction and accumulation of lawsonite eclogite and garnet blueschist in eastern Australia. *J. Metamorphic Geol.* **38**, 157–182.

Tamblyn R., Hand M., Morrissey L., Zack T., Phillips G. and Och D. (2020) Resubduction of lawsonite eclogite within a serpentinite-filled subduction channel. *Contrib. Mineral. Pet.* **175**, 74.

Tardani D., Reich M., Deditius A. P., Chryssoulis S., Sánchez-Alfaro P., Wrage J. and Roberts M. P. (2017) Copper-arsenic decoupling in an active geothermal system: A link between pyrite and fluid composition. *Geochim. Cosmochim. Acta* **204**, 179–204.

Taetz S., John T., Bröcker M., Spandler C. and Stracke A. (2018) Fast intraslab fluid-flow events linked to pulses of high pore fluid pressure at the subducted plate interface. *Earth Planet. Sci. Lett.* **482**, 33–43.

Tassara S., González-Jiménez J. M., Reich M., Schilling M. E., Morata D., Begg G., Saunders E., Griffin W. L., O'Reilly S. Y., Grégoire M., Barra F. and Corgne A. (2017) Plume-subduction interaction forms large auriferous provinces. *Nat. Comm.* **8**, 1–8.

Tassara S., González-Jiménez J. M., Reich M., Saunders E., Luguet A., Morata D., Grégoire M., van Acken D., Schilling M. E., Barra F., Nowell G. and Corgne A. (2018) Highly siderophile elements mobility in the subcontinental lithospheric mantle beneath southern Patagonia. *Lithos* **314–315**, 579–596.

Timm C., de Ronde C. E. J., Leybourne M. W., Layton-Matthews D. and Graham I. J. (2012) Sources of chalcophile and

siderophile elements in Kermadec Arc lavas. *Econ. Geol.* **107**, 1527–1538.

Tomkins A. G. and Evans K. A. (2015) Separate zones of sulfate and sulfide release from subducted mafic oceanic crust. *Earth Planet. Sci. Lett.* **428**, 73–83.

Tracy R. J. and Robinson P. (1988) Silicate-sulfide-oxide-fluid reactions in granulite-grade pelitic rocks, central Massachusetts. *Am. J. Sci.* **288-A**, 45–74.

Tsujimori T. and Ernst W. G. (2014) Lawsonite blueschists and lawsonite eclogites as proxies for paleo-subduction zone processes: A review. *J. Met. Geol.* **32**, 436–454.

Tsujimori T. and Mattinson C. (2021) Eclogites in different tectonic settings. In *Encyclopedia of Geology* (eds. D. Alderton and S. A. Elias), 2nd ed. Academic Press, United Kingdom, pp. 561–568.

van der Straaten F., Schenk V., John T. and Gao J. (2008) Blueschist-facies rehydration of eclogites (Tianshan, NW-China): Implications for fluid-rock interaction in the subduction channel. *Chem. Geol.* **255**, 195–219.

van der Straaten F., Halama R., John T., Schenk V., Hauff F. and Andersen N. (2012) Tracing the effects of high-pressure metasomatic fluids and seawater alteration in blueschist-facies overprinted eclogites: Implications for subduction channel processes. *Chem. Geol.* **292–293**, 69–87.

Viete D. R., Hacker B. R., Allen M. B., Seward G. G. E., Tobin M. J., Kelley C. S., Cinque G. and Duckworth A. R. (2018) Metamorphic records of multiple seismic cycles during subduction. *Science Adv.* **4**, 1–14.

Vitale Brovarone A., Alard O., Beyssac O., Martin L. and Picatto M. (2014) Lawsonite metasomatism and trace element recycling in subduction zones. *J. Met. Geol.* **32**, 489–514.

Walters J. B., Cruz-Uribe A. M. and Marschall H. R. (2019) Isotopic compositions of sulfides in exhumed high-pressure terranes: Implications for sulfur cycling in subduction zones. *Geochem. Geophys. Geosys.* **20**, 1–28.

Walters J. B., Cruz-Uribe A. M. and Marschall H. R. (2020) Sulfur loss from subducted altered oceanic crust and implications for mantle oxidation. *Geochem. Perspect. Lett.* **13**, 36–41.

Whitney D. L., Fornash K. F., Kang P., Ghent E. D., Martin L., Okay A. I. and Vitale Brovarone A. (2020) Lawsonite composition and zoning as tracers of subduction processes: A global review. *Lithos* **370–371** 105636.

Whitney D. L. and Evasns B. W. (2010) Abbreviations for names of rock-forming minerals. *Am. Mineral.* **95**, 185–187.

Wilson S. A., Ridley W. A. and Koenig A. E. (2002) Development of sulfide calibration standard for the laser ablation inductively-coupled plasma mass spectrometry technique. *J. Analyt. Atom. Spect.* **17**, 406–409.

Wu Y. F., Fougerouse D., Evans K., Reddy S. M., Saxey D. W., Guagliardo P. and Li J. W. (2019) Gold, arsenic, and copper zoning in pyrite: A record of fluid chemistry and growth kinetics. *Geology* **47**, 641–644.

Yardley B. W. D., Rochelle C. A., Barnicoat A. C. and Lloyd G. E. (1991) Oscillatory zoning in metamorphic minerals: An indicator of infiltration metasomatism. *Mineral. Mag.* **380**, 357–365.

Yi W., Halliday A. N., Alt J. C., Lee D.-C., Rehkämper M., Garcia M. O., Langmuir C. H. and Su Y. (2000) Cadmium, indium, tin, tellurium, and sulfur in oceanic basalts: Implications for chalcophile element fractionation in the Earth. *J. Geophys. Res.* **105**, 927–949.

Zack T., Kronz A., Foley S. F. and Rivers T. (2002) Trace element abundances in rutiles from eclogites and associated garnet mica schists. *Chem. Geol.* **184**, 97–122.

Associate editor: Martin Reich